

Resubmitted to ApJ on August 18, 2006

A New Method for Isolating M31 Red Giant Stars: The Discovery of Stars out to a Radial Distance of 165 Kiloparsecs

Karoline M. Gilbert¹, Puragra Guhathakurta¹, Jasonot S. Kalirai^{1,2}, R. Michael Rich³, Steven R. Majewski⁴, James C. Ostemheimer⁴, David B. Reitzel³, A. Javier Cenarro^{1,5}, Michael C. Cooper⁶, Carynn Luine¹, and Richard J. Patterson⁴

kgilbert@astro.ucsc.edu, raja@ucolick.org, jkalirai@ucolick.org,
rmar@astro.ucla.edu, srm4n@virginia.edu, jostheim@alumni.virginia.edu,
reitzel@astro.ucla.edu, cen@astrax.fis.ucm.es, cooper@astron.berkeley.edu,
kierrica@hotmail.com, rjp0i@virginia.edu

ABSTRACT

We present a method for isolating a clean sample of red giant branch stars in the outer regions of the Andromeda spiral galaxy (M31). Our study is based on an ongoing spectroscopic survey using the DEIMOS instrument on the Keck II 10-m telescope⁷. The survey aims to study the kinematics, global structure, substructure, and metallicity of M31's halo. Although most of our spectroscopic targets were photometrically screened to reject foreground Milky Way dwarf star contaminants, the latter class of objects still constitutes a substantial fraction of

¹UCO/Lick Observatory, Department of Astronomy & Astrophysics, University of California Santa Cruz, 1156 High Street, Santa Cruz, California 95064, USA.

²Hubble Fellow.

³Department of Physics & Astronomy, Knudsen Hall, University of California, Los Angeles, California 90095, USA.

⁴Department of Astronomy, University of Virginia, PO Box 3818, Charlottesville, Virginia 22903, USA.

⁵Present address: Departamento de Astrofísica, Universidad Complutense de Madrid, E-28040 Madrid, Spain.

⁶Department of Astronomy, Campbell Hall, University of California, Berkeley, California 94720, USA.

⁷Data presented herein were obtained at the W. M. Keck Observatory, which is operated as a scientific partnership among the California Institute of Technology, the University of California and the National Aeronautics and Space Administration. The Observatory was made possible by the generous financial support of the W. M. Keck Foundation.

the observed spectra in the sparse outer halo. Our likelihood-based method for isolating M31 red giants uses five criteria: (1) radial velocity, (2) photometry in the intermediate-width DDO51 band to measure the strength of the MgH/Mg *b* absorption features, (3) strength of the Na I 8190 Å absorption line doublet, (4) location within an (*I*, *V* – *I*) color-magnitude diagram, and (5) comparison of photometric (CMD-based) versus spectroscopic (Ca II 8500 Å triplet-based) metallicity estimates. We also discuss other giant/dwarf separation criteria that might be useful in future analyses: the strength of the K I absorption lines at 7665 and 7699 Å and the TiO bands at 7100, 7600, and 8500 Å. Training sets consisting of definite M31 red giants and Galactic dwarf stars are used to derive empirical probability distribution functions for each diagnostic. These functions are used to calculate the likelihood that a given star is a red giant branch star in M31 versus a Milky Way dwarf star. By applying this diagnostic method to our spectroscopic data set, we isolate 40 M31 red giants beyond a projected distance of $R = 60$ kpc from the galaxy’s center, including three red giants out at $R \sim 165$ kpc. The ability to identify individual M31 red giant stars gives us an unprecedented level of sensitivity in studying the properties of the galaxy’s outer halo.

Subject headings: galaxies: halo — galaxies: individual (M31) — techniques: spectroscopic

1. Introduction

Hierarchical galaxy formation theories propose that galaxies are built up through the accretion of smaller systems (Searle & Zinn 1978; White & Rees 1978). Lately there has been significant progress in the investigation of galactic halos, especially in studies focusing on the contribution of tidal debris from disrupted satellites. Computational studies, using numerical simulations and semi-analytic modelling, have made great strides in understanding the properties of halos built up from tidal debris (e.g., Johnston, Hernquist, & Bolte 1996; Johnston 1998; Helmi & White 1999; Helmi & de Zeeuw 2000; Bullock, Kravtsov, & Weinberg 2001; Bullock & Johnston 2005). Recent observational studies have led to the discovery of large tidal streams in the Milky Way (MW) halo such as the Magellanic Stream (Mathewson, Cleary, & Murray 1974), the Sagittarius stream (Ibata, Gilmore, & Irwin 1994; Majewski et al. 2003; Newberg et al. 2003), and the Monoceros stream (Yanny et al. 2003; Rocha-Pinto et al. 2003). These observations are adding new insight to the study of halo formation.

Studies of tidal structures in the halo of the Galaxy present inherent difficulties, as

they generally require wide-field surveys given their large angular extent when viewed from our vantage point within the disk. The Andromeda spiral galaxy (M31) presents a unique opportunity to study a galaxy like our own from an external perspective. In addition, it has the advantage of having a high disk inclination angle of 78° (de Vaucouleurs 1958; Walterbos & Kennicutt 1988), and at a distance of 783 kpc (Stanek & Garnavich 1998; Holland 1998) it is close enough to allow detailed photometric studies of individual stars (e.g., Mould & Kristian 1986; Durrell, Harris, & Pritchett 2001, 2004; Bellazzini et al. 2003), even faint main-sequence turnoff stars (Brown et al. 2003, 2006), as well as spectroscopy of individual red giant branch (RGB) stars (Reitzel & Guhathakurta 2002; Reitzel, Guhathakurta, & Rich 2004; Ibata et al. 2004, 2005; Guhathakurta et al. 2006; Kalirai et al. 2006b; Chapman et al. 2006).

As in the MW, recent studies of M31 have uncovered evidence of past and present accretion events. Star-count maps covering a large area of M31 have revealed a ‘giant southern stream’ and many other signs of disturbance in the spheroid and outer disk (Ibata et al. 2001; Ferguson et al. 2002). Evidence of tidal disruption in M31’s closest satellite galaxies M32 and NGC 205 has been presented by Choi et al. (2002).

In order to investigate the substructure of the outer halo through kinematics and metallicity, we have undertaken a spectroscopic survey of the M31 halo with the Deep Imaging Multi-Object Spectrograph (DEIMOS; Faber et al. 2003) on the Keck II Telescope. The first results from this survey focus on the giant southern stream discovered by Ibata et al. (2001), and are presented by Guhathakurta et al. (2006), Font et al. (2006), and Kalirai et al. (2006b).

The ability to take spectra of individual stars in the halo of M31 opens up many exciting avenues for studying its kinematics, structure, and metallicity (Guhathakurta et al. 2006; Kalirai et al. 2006b). Radial velocities are the standard method for discriminating between RGB stars in M31 and dwarf stars in the MW. However, the radial velocity distributions of these two populations overlap. Although modelling the distribution of radial velocities can provide a *statistical* separation of M31 RGB versus Galactic dwarf stars, a more stringent method for differentiating the two populations is needed to mark individual stars as M31 RGB or MW dwarf stars. This is vital for studying the far outer regions of the halo, where our survey is expected to find only a handful (if any) RGB stars per DEIMOS pointing, and will give us the sensitivity needed to probe M31’s halo to extremely low surface brightness levels.

In this paper, we describe a method that uses a combination of spectroscopic and photometric information to determine whether a star is an M31 RGB star or a foreground MW dwarf star. This allows us to isolate a clean sample of RGB stars in M31. Details of the

observations and data reduction are summarized in § 2. The selection of training set stars, the different spectroscopic and photometric diagnostics, probability distribution functions, and the application of a likelihood-based screening technique are described in § 3. In § 4, the robustness of the diagnostic method is tested and it is compared to other methods used to study RGB stars in M31. The main points of the paper are summarized in § 5.

2. Data

2.1. Slitmask Design and Observations

Objects were selected for Keck/DEIMOS spectroscopy using the M31 photometry/astrometry catalogs of Ostheimer (2002). The catalogs were derived from images taken with the Mosaic camera on the Kitt Peak National Observatory (KPNO)⁸ 4-m telescope in the Washington System M and T_2 bands and the intermediate-width DDO51 band. The DDO51 filter is centered at a wavelength of 5150 Å with a width of about 100 Å. It includes the surface-gravity sensitive Mg b and MgH stellar absorption features, which are strong in dwarf stars but weak in RGB stars. Photometric transformation relations from Majewski et al. (2000) were used to derive Johnson-Cousins V and I magnitudes from the M and T_2 magnitudes.

Due to the sparseness of RGB stars the outer halo of M31, objects were photometrically pre-selected in order to maximize the efficiency of the spectroscopic observations. Each object was assigned a DDO51 parameter, an estimate of the probability of its being an RGB star based on its position in the $(M - DDO51)$ versus $(M - T_2)$ color-color diagram (Palma et al. 2003). Objects with point-like morphology (based on the DAOPHOT-based morphological parameters `chi` and `sharp`) and large values of the DDO51 parameter were given the highest priority during the design of the DEIMOS slitmask. Background galaxies tend to get assigned high values of the DDO51 parameter (either because their Mg b /MgH features are redshifted out of the DDO51 band or because they are dominated by light from RGB stars), but all but the most compact ones fail the `chi` and `sharp` criteria. Guhathakurta et al. (2006) presents details of the spectroscopic target selection and slitmask design for the outer halo fields in our survey.

In addition to outer halo fields, we have obtained Keck/DEIMOS observations of three fields relatively close to the center of M31 that have recently been imaged to below the

⁸Kitt Peak National Observatory of the National Optical Astronomy Observatory is operated by the Association of Universities for Research in Astronomy, Inc., under cooperative agreement with the National Science Foundation

main sequence turnoff with the Advanced Camera for Surveys on the *Hubble Space Telescope* (Brown et al. 2003, 2006). These fields are on the southeastern minor axis (H11), giant southern stream (H13s), and northeastern major axis (H13d). We do not have DDO51/Washington system photometry for these fields so we did not use the P_{giant} criterion for spectroscopic target selection. The surface density of M31 RGB stars is very high in these inner fields, leading to a large RGB to dwarf ratio even without preselection of RGB star candidates. Photometry for the H11 and H13s fields comes from MegaCam images taken with the 3.6-m Canada-France-Hawaii Telescope (CFHT)⁹ in the g' and i' bands. Object detection and photometry for these fields was done using SExtractor (Bertin & Arnouts 1996) and the instrumental magnitudes were transformed to the Johnson-Cousins V and I bands (Kalirai et al. 2006b). Photometry for the H13d fields comes from short Keck/DEIMOS imaging exposures in the V and I bands (Reitzel et al. 2006, in preparation). The lists for slitmask design in the H11, H13s, and H13d fields were based on I magnitude and the SExtractor morphological criterion **stellarity**.

Spectroscopic observations of DEIMOS multislit masks were obtained in fall 2002, 2003, 2004, and 2005 (Table 1; Fig. 1) using the Keck II telescope and the DEIMOS instrument with the 1200 line mm^{-1} grating. This grating yields a dispersion of $0.33 \text{ \AA pix}^{-1}$ and the spatial scale is $0''.12 \text{ pix}^{-1}$. For masks observed in fall 2002, the central wavelength setting was $\lambda 8550 \text{ \AA}$, and the spectra cover the range $\lambda\lambda 7200\text{--}9900 \text{ \AA}$. This setting had the unfortunate effect that one of the lines of the Ca II triplet occasionally landed in the inter-CCD gap in DEIMOS. To avoid this, and to extend the spectral coverage to shorter wavelengths to include the $\lambda 7100 \text{ \AA}$ TiO and $\lambda 6563 \text{ \AA}$ H α features, masks observed in fall 2003, 2004, and 2005 had the central wavelength set to $\lambda 7800 \text{ \AA}$, yielding the spectral coverage $\lambda\lambda 6450\text{--}9150 \text{ \AA}$. Slits had a width of $1''$, which subtends 4.8 pix. The spectral resolution is slightly better than this: $3.8 \text{ pix} = 1.26 \text{ \AA}$ for the typical seeing conditions ($0''.8$ FWHM). This resolution corresponds to 44 km s^{-1} at the Ca II triplet. Our actual radial velocity measurement error is significantly smaller than this (see § 2.3)—the centroiding accuracy depends on the signal-to-noise (S/N) ratio and is typically much smaller than the width of the line (Tonry & Davis 1979).

⁹MegaPrime/MegaCam is a joint project of CFHT and CEA/DAPNIA, at the Canada-France-Hawaii Telescope which is operated by the National Research Council of Canada, the Institut National des Science de l'Univers of the Centre National de la Recherche Scientifique of France, and the University of Hawaii.

Table 1: Details of spectroscopic observations and basic results.

Mask	Pointing center:		PA	# Sci. targets ^a	Date of Obs. (UT)	Number of $Q = -2/1/2/3/4$ cases
	α_{J2000} ($^{\text{h}}:\text{m}:\text{s}$)	δ_{J2000} ($^{\circ}:\text{':}:\text{''}$)	($^{\circ}$ E of N)			
H11_1	00:46:21.02	+40:41:31.3	21.0	139	2004 Sep 20	40/01/29/10/59 ^b
H11_2	00:46:21.02	+40:41:31.3	-21.0	138	2004 Sep 20	03/00/55/10/70
H13s_1	0:44:14.76	+39:44:18.2	21.0	134	2004 Sep 20	05/01/58/16/54
H13s_2	0:44:14.76	+39:44:18.2	-21.0	138	2004 Sep 20	44/00/33/11/50 ^b
H13d_1	0:49:04.80	+42:45:22.6	27.8	146	2004 Sep 20	01/01/41/22/81
H13d_2	0:49:04.80	+42:45:22.6	27.8	144	2004 Sep 20	00/01/34/20/89
a3_1	00:48:21.16	+39:02:39.2	64.2	85	2002 Aug 16	08/22/14/15/26
a3_2	00:47:47.24	+39:05:56.3	178.2	81	2002 Oct 11	07/19/14/09/32
a3_3	00:48:23.17	+39:12:38.5	270.0	83	2003 Oct 26	02/00/22/11/48
a0_1	00:51:51.32	+39:50:21.4	-17.9	89	2002 Aug 16	05/00/35/11/38
a0_2	00:51:29.59	+39:44:00.8	90.0	89	2002 Oct 12	02/00/42/15/30
a0_3	00:51:50.46	+40:07:00.9	0.0	90	2004 Jun 17	07/01/24/10/47
a13_1	00:42:58.34	+36:59:19.3	0.0	80	2003 Sep 30	07/04/08/05/56
a13_2	00:41:28.27	+36:50:19.2	0.0	71	2003 Sep 30	03/01/05/02/60
a19_1	00:38:16.05	+35:28:07.2	-90.0	71	2005 Aug 29	03/00/04/06/58
m6_1	01:09:51.75	+37:46:59.8	0.0	75	2003 Oct 1	04/01/05/04/61
m6_2	01:08:36.22	+37:28:59.6	0.0	72	2005 Jun 9	05/01/05/12/49
b15_1	00:53:23.63	+34:37:16.0	-90.0	65	2005 Sep 7	07/00/07/08/43
b15_3	00:53:37.77	+34:50:04.1	-90.0	74	2005 Sep 7	05/02/09/04/54
m8_1	01:18:11.56	+36:16:24.9	0.0	56	2005 Jul 7	03/00/03/02/48
m8_2	01:18:35.87	+36:14:30.9	0.0	59	2005 Jul 7	03/00/04/07/45
m11_1	01:29:34.44	+34:13:45.4	0.0	72	2003 Sep 30	05/03/10/07/47
m11_2	01:29:34.35	+34:27:45.5	0.0	68	2003 Oct 1	04/03/17/02/42
m11_3	01:30:01.53	+34:13:45.4	0.0	80	2005 Jul 8	01/03/11/12/53
m11_4	01:30:37.33	+34:13:27.4	0.0	75	2005 Jul 8	02/02/10/10/51

^aA number of stars were observed on two different masks (§ 2.3).^bThe high number of failed targets in these masks reflects incomplete data reduction for these masks. Our success rate for these masks will increase once the remaining slits are reduced.

2.2. Spectroscopic Data Reduction

Spectra were reduced using the `spec2d` and `spec1d` software developed by the DEEP2 team at the University of California, Berkeley¹⁰. Spectra were flat fielded and corrected for fringing, and a wavelength solution was determined from arc lamp exposures. Each slit was sky subtracted, and individual exposures were averaged using cosmic-ray rejection and inverse-variance weighting. Extracted one-dimensional spectra were cross-correlated against stellar and galaxy templates spanning a range of spectral types to determine the redshift. The ten best cross-correlation matches were reported by the `spec1d` pipeline. These matches were evaluated by eye using the visual inspection software `zspec` [developed by D. Madgwick and one of us (M.C.C.) for the DEEP2 survey] and the best one identified. In rare cases, the correct redshift did not appear among the top ten cross-correlation matches in spite of the presence of one or more visually identifiable spectral features [such as the Ca II triplet, Na I doublet (dwarf stars), and $\lambda 7100$ Å TiO band]; the redshift had to be determined manually in these cases. Each spectrum was assigned a quality code: spectra with secure redshifts was assigned $Q = 4$ (at least two good spectral lines) or $Q = 3$ (one good line and one marginal line). Objects for which the spectra did not yield a reliable redshift were assigned $Q = 2$ (visible continuum with low S/N or no lines), $Q = 1$ (very weak and/or undetectable continuum), or $Q = -2$ (catastrophic instrument failure). We make no distinction between $Q = 4$ and $Q = 3$ spectra in our analysis. Table 1 lists the number of targets per quality bin for each mask. For more details about the reduction of the survey data see Guhathakurta et al. (2006).

Spectra which have secure redshift measurements ($Q = 4$ or 3) are shifted to the rest frame and rebinned onto a common, uniform (linear) wavelength grid. The continuum level of each spectrum is normalized to unity and the S/N computed in the region of the Ca II triplet (both the overall S/N and the S/N between strong atmospheric emission lines). The S/N calculation is based on the assumption of Poisson errors as reported by `spec2d` for each wavelength element; the lack of flexure and fringing in DEIMOS allows one to achieve Poisson-limited sky subtraction. Finally, the spectra are smoothed by a 10 pixel boxcar in wavelength weighted by their inverse variance. Line strength [equivalent width (EW)] measurements are performed on the normalized spectra using a measurement window centered on the absorption feature (e.g., Na I doublet at 8190 Å) with continuum windows on each side of the feature (see Table 3). Details of the EW measurements are provided in the individual diagnostic sections (e.g., § 3.2.4). The measured stellar radial velocities are

¹⁰<http://astron.berkeley.edu/~cooper/deep/spec1d/primer.html>,
<http://astron.berkeley.edu/~cooper/deep/spec2d/primer.html>

corrected to heliocentric velocities using the IRAF¹¹ task RVCOR.

2.3. Empirical Error Estimates from Duplicate Measurements

In some of our survey fields, masks were designed to overlap, allowing for repeat observations of a total of 84 objects. The duplicate measurements allow us to make empirical estimates of the errors in the velocity and line widths measured from the spectra. Most of the 84 duplicate measurements with successful redshifts are from field H13d (61). There are 9 duplicate measurements with successful redshifts in field a0, 8 in field a3, and 2 each in fields H11 and H13s. For each pair of spectra, the difference in the EW estimates (or radial velocity estimates) between the two masks is calculated. The measurement error is assumed to be proportional to the inverse of the S/N of the spectrum:

$$\sigma_i = C \left(\frac{N}{S} \right)_i . \quad (1)$$

We define

$$X_{ij} = \frac{(EW)_i - (EW)_j}{C \sqrt{\left(\frac{N}{S} \right)_i^2 + \left(\frac{N}{S} \right)_j^2}} \quad (2)$$

so that for the correct value of C , the distribution of X_{ij} 's will be a Gaussian of unit width. For each quantity measured from the spectra, Table 2 lists the error in that quantity for a S/N of 10, which is typical of the spectra in our sample (see Table 3 for index definitions).

In addition to providing empirical error estimates for line width and radial velocity measurements, the duplicate spectra were co-added to achieve higher S/N for measurement of the spectral features. During coaddition, the individual spectra were weighted according to the measured inverse variance for each pixel.

3. Method for Selecting a Clean Sample of M31 Red Giants

To isolate a clean sample of RGB stars, we calculate empirical probability distribution functions (PDFs) based on the properties of known RGB and dwarf stars. Each star is assigned individual probabilities of being an M31 RGB or a MW dwarf star based on its

¹¹IRAF is distributed by the National Optical Astronomy Observatory, which is operated by the Association of Universities for Research in Astronomy, Inc., under cooperative agreement with the National Science Foundation.

Table 2: Empirical error estimates of quantities measured from the spectra, $C(N/S)$, for our typical S/N of 10.

Quantity	Typical Error
Velocity	17 km s ⁻¹
Na I EW	0.74 Å
Ca II EW (Σ Ca)	1.09 Å
[Fe/H] _{spec}	0.46 dex
K ₇₆₆₅ EW	1.4 Å
K ₇₆₉₉ EW	0.6 Å
TiO ₇₁₀₀ EW	0.07 Å
TiO ₇₆₀₀ (1) EW	0.05 Å
TiO ₇₆₀₀ (2) EW	0.1 Å
TiO ₇₆₀₀ (3) EW	0.3 Å
TiO ₇₆₀₀ (comb) EW	0.2 Å
TiO ₈₅₀₀ EW	0.1 Å

location within each of the diagnostics. The probabilities from the first five diagnostics are then combined to give an overall likelihood that the star is an RGB star in M31 or a foreground dwarf star contaminant. The selection of RGB and dwarf star training sets, the diagnostics, construction of the PDFs, and the final likelihood-based method are described below.

3.1. Training Set Selection

The DDO51-based preselection procedure we have used to select spectroscopic targets is very effective at eliminating foreground MW dwarf stars in the color range $1 \lesssim (V - I)_0 \lesssim 2$, but is less effective outside this color range (see § 4.1.1 and § 4.1.2). This non-uniformity in the dwarf rejection probability as a function of color would be difficult to characterize in a model training set. We have therefore chosen to use *empirical* RGB and dwarf training sets. Since our PDFs for each diagnostic are empirically determined, the selection of unbiased and largely uncontaminated training sets is important. Initial training set stars were drawn from all fields observed during the 2002–2004 observing runs except field H13d, due to the difficulty in separating out M31 disk stars from Galactic dwarfs on the northeastern major axis (disk field).

The initial RGB training set stars were picked mainly on the basis of radial velocity: $v <$

-300 km s^{-1} (the systemic velocity of M31). While it is possible for MW halo stars to have a heliocentric radial velocity this negative, the expected fraction in our overall data set is very small. The initial dwarf training set had to be chosen more carefully, since the radial velocity distribution of M31 spheroid stars significantly overlaps the dwarf velocity distribution. We included all stars which had been commented as having strong Na I absorption during the data reduction phase. Stars with radial velocities $v > -200 \text{ km s}^{-1}$ in fields with a clear RGB/dwarf bimodality in the radial velocity distribution were also included in the dwarf training sets. Finally, we included all the stars in field m11, since its large distance from M31 ($R \sim 165 \text{ kpc}$ in projection) makes it extremely unlikely for it to contain RGB stars based on previous estimates of the surface brightness profile of M31's halo (Pritchett & van den Bergh 1994).

The initial training sets were used to calculate preliminary PDFs and probabilities for all stars from the 2002–2004 observing runs. We used these preliminary RGB and dwarf probability estimates to isolate stars that have a much higher combined probability (summed over the first five diagnostics) of being an RGB star than a dwarf star. These stars comprise our final RGB star training set. A similar procedure was used to construct our final dwarf star training set. These final RGB and dwarf star training sets, consisting of a few hundred stars each, were used to refine the PDFs for each diagnostic.

Given that a simple velocity cut alone is not enough to isolate a clean sample of M31 RGB stars in the outer halo, it is worth explaining why we use a velocity cut to select stars for the (initial) RGB training set:

- The velocity cut used to define the initial RGB training set, $v < -300 \text{ km s}^{-1}$ ($v < v_{\text{sys}}^{\text{M31}}$), is very extreme. In fact, only half of all the M31 RGB stars in our sample are expected to survive this cut. This is acceptable for the RGB training set, which only needs to be a representative set of M31 RGB stars, not necessarily a complete one. However, such a cut would adversely affect our ability to find (and analyze the dynamics of) RGB stars in M31's sparse outer halo.
- There is a small but finite probability ($\lesssim 1\%$) of encountering a MW dwarf whose radial velocity is $v < -300 \text{ km s}^{-1}$. In the outermost fields (e.g., field m11), where our sample includes of order 100 MW dwarfs, this can translate to a few dwarf stars satisfying the velocity cut. This is of the same order as the number of M31 RGB stars found in these fields (see § 3.5, § 4.4, and Table 5). Thus, even this extreme velocity cut would lead to a large MW dwarf contamination rate if we were to use it to search for M31 RGB stars in the outer fields. By contrast these few MW dwarfs comprise a negligible fraction ($\ll 1\%$) of the RGB training set; most RGB training set stars come

from the inner fields where the surface density of M31 RGB stars greatly exceeds that of MW dwarf stars.

To summarize, the initial training sets were based on extreme cuts in a single parameter: radial velocity, Na line strength, or sky position. This resulted in limited, slightly contaminated, and somewhat biased sets of RGB and dwarf stars. By contrast, the final training sets were based on cuts in the combined probability ratio. Since this probability ratio combines information from various parameters, the final training sets are more complete, less contaminated, and less biased than the initial training sets.

The plots for the first five diagnostics below (Figs. 2–5) show the initial training set stars overlaid on the final PDFs. The fact that our PDFs did not change drastically when we switched from the initial to final training sets suggests that our training sets are stable. We investigate our MW dwarf star training set for possible biases by exploring the relationships between the different parameters in § 4.2.3. The different properties of M31 RGB training set stars — Na₁ EW, K₁ EW, TiO EW, $(V - I)_0$ color, DDO51 parameter, CMD position, and [Fe/H]_{phot} versus [Fe/H]_{spec} — have no detectable dependence on radial velocity.

3.2. Diagnostics

3.2.1. Method for Constructing Analytic Probability Distribution Functions

For each diagnostic, analytic PDFs are calculated for each of the M31 RGB and MW dwarf star training sets. In this section we describe the general process of computing analytic PDFs; subsequent sections describe the specific functions used for each diagnostic. For the one-dimensional distributions (radial velocity and DDO51 parameter) an analytic function was fit to the training set's distribution and normalized. The PDFs for the two-dimensional distributions (Na₁ EW, K₁ EW, and TiO EW vs. $(V - I)$ color, CMD position, and [Fe/H]_{phot} versus [Fe/H]_{spec}) are also determined using an analytic fitting scheme. The distribution of the data along both the x and y axes must be included in the final PDF. In modeling the two-dimensional PDF, the y distribution is treated as a Gaussian whose mean and rms depend on x . For each training set, we compute the mean and rms of the y distribution for several bins in x : $\langle y \rangle_i$ and σ_i^y as a function of x_i , where x_i is the mean value in each bin. Analytic functions are then fit to the measured $\langle y \rangle_i$ and σ_i^y values, which are denoted as $\langle y \rangle_{\text{fit}}(x)$ and $\sigma_{\text{fit}}^y(x)$, respectively. This describes how the training set's y values are distributed as a function of x , but does not contain information about the distribution of x values of the training set. We therefore also fit a smooth analytic function $P(x)$ to the projection of the training set distribution along the x axis. Finally, the analytic two-dimensional PDF is

defined as:

$$\text{PDF}(x, y) = C \ P(x) \ \exp \left[-0.5 \ [y - \langle y \rangle_{\text{fit}}(x)]^2 / [\sigma_{\text{fit}}^y(x)]^2 \right] \quad (3)$$

where C is a normalization constant such that the PDF integrates to unity.

3.2.2. Radial Velocities

The radial velocity PDFs and histograms of the training set data are shown in Figure 2. Due to the DDO51 pre-selection technique employed in our survey (§ 2.1), dwarf distributions from standard Galactic models (e.g., Bahcall & Soneira 1984; Ratnatunga & Bahcall 1985; Reitzel & Guhathakurta 2002) cannot directly be used for our data set. The dwarf training set shows an asymmetric distribution, and the sum of two Gaussians was fit to the heliocentric radial velocity distribution of the dwarf training set (§ 2.2). The initial RGB training set was chosen on the basis of radial velocity measurements, therefore it could not be used to define the RGB velocity PDF. In addition, many of the observed fields have significant substructure or small number statistics, making it difficult to choose an alternate training set without biases. Instead, we adopted a Gaussian centered on the systemic velocity of M31 to define the RGB radial velocity PDF: $\langle v_{\text{hel}} \rangle = -300 \text{ km s}^{-1}$ and $\sigma = 85 \text{ km s}^{-1}$. This is based on a fit to our (admittedly limited) sample in H11, our smoothest spheroid field. As shown in Figure 2, there is significant overlap between the RGB and dwarf distributions, which makes it difficult to differentiate between RGB and dwarf stars on the basis of radial velocity alone. We will return to this issue in § 4.4.

Our adopted velocity dispersion of 85 km s^{-1} is probably not representative of the entire M31 spheroid; previously published values are at least as large as this (Reitzel & Guhathakurta 2002; Guhathakurta et al. 2006; Chapman et al. 2006). The velocity dispersion of M31’s outer halo ($R \gtrsim 50 \text{ kpc}$) remains poorly constrained at the present time. It should be noted that the Gaussian sigma of 85 km s^{-1} is only used for the definition of the RGB radial velocity PDF; we are *not* suggesting that this be used as a model for the M31 bulge/halo. Use of a larger sigma value would result in a higher value for the RGB PDF in the overlap region between MW dwarf and M31 RGB velocity distributions. Thus, our adopted dispersion of 85 km s^{-1} represents a conservative choice.

In fields where a skewed distribution of M31 RGB velocities results in greater overlap with the MW dwarf velocity distribution, the RGB velocity PDF can be modified to account for this. For example, the stellar disk of M31 is apparent as a dynamically cold peak in the radial velocity histogram of our NE major-axis field H13d. We use the sum of two Gaussians to model the M31 disk and spheroid populations in that field. The rest of our fields show

no evidence of a contribution from the extended stellar disk discussed by Ibata et al. (2005). This is not surprising given that most of our fields are located at large distances from M31’s center and/or lie close to its SE minor axis (Kalirai et al. 2006a).

3.2.3. *DDO51 Distribution*

The location of a star in $(M - DDO51)$ versus $(M - T_2)$ color-color space was used to assign it a DDO51 parameter (§ 2.1; Palma et al. 2003). Values of the DDO51 parameter close to 1 indicate that the star is probably an M31 RGB star while values close to 0 indicate it is probably a foreground MW dwarf star. The DDO51 parameter was used to assign priorities to objects during the slitmask design, and it can also be used to help differentiate between RGB and dwarf stars independent of the spectroscopic data. (In order to fill the masks to the fullest extent possible, some objects with low DDO51 parameters were observed.) Figure 3 shows the PDFs and the initial training sets. The dwarf training set was fit by a double exponential, and the RGB training set was fit by a single exponential. For both dwarf and RGB stars, the training sets are reduced in number relative to the other diagnostics because DDO51 photometry was not available for fields H11, H13s or H13d. As in the case of the radial velocity diagnostic, there is some overlap between the RGB and dwarf PDFs.

3.2.4. *Na I Equivalent Width*

The EW of the Na I absorption line at $\lambda = 8190.5$ Å is dependent on both surface gravity and temperature, making it likely to be a useful dwarf/RGB star discriminator (Schiavon et al. 1997). Table 3 contains details of the EW measurement.

This diagnostic relies on the distribution of stars in $(V - I)_0$ color versus Na I EW space. Distributions in each quantity were fit analytically. The dwarf star training set’s $(V - I)_0$ color distribution was fit by a double Gaussian and the RGB star training set’s $(V - I)_0$ color distribution was fit by a Gaussian plus an exponential. Each training set was then divided into bins according to $(V - I)_0$ color and the mean and rms of the Na I EW was calculated for each bin. Piecewise linear fits were made to the mean Na I EW vs. $(V - I)_0$ and to the rms Na I EW vs. $(V - I)_0$. The Na I EW distribution can be characterized by Gaussians with running mean and sigma values based on the linear fits. The analytic fit to the $(V - I)_0$ distribution was multiplied by the (running) Gaussian fit to the Na I EW distribution to construct the two-dimensional PDF. In other words, x and y were set to $(V - I)_0$ color and Na I EW, respectively, in the context of § 3.2.1 and Eqn. 3.

Table 3: Absorption line-strength index definitons used in this work.

Index	Type ^a	Main	Continuum
		Bandpass (Å)	Bandpasses (Å)
Na I	<i>g a</i>	8179–8200	8130–8175, 8210–8220
Ca II ₈₄₉₈	<i>g a</i>	8489–8507	8560–8644
Ca II ₈₅₄₂	<i>g a</i>	8533–8551	8560–8644
Ca II ₈₆₆₂	<i>g a</i>	8653–8671	8560–8644
K ₇₆₆₅	<i>g a</i>	7660–7670	7677–7691, 7728–7741, 7764–7784, 7802–7825, 7877–7895
K ₇₆₉₉	<i>g a</i>	7694–7703	7677–7691, 7728–7741, 7764–7784, 7802–7825, 7877–7895
TiO ₇₁₀₀	<i>c a</i>	7055–7245	7012–7048, 7512–7576
TiO ₇₆₀₀ (1)	<i>c a</i>	7700–8000	7500–7580, 8080–8170
TiO ₇₆₀₀ (2)	<i>c a</i>	7736–7810	7500–7580, 8080–8170
TiO ₇₆₀₀ (3)	<i>g s</i>	none	7721–7748, 7802–7826, 7878–7895, 7963–7986, 8001–8024, 8086–8113
TiO ₈₅₀₀	<i>g s</i>	none	8474–8484, 8563–8577, 8619–8642, 8700–8725, 8776–8792

^aTypes *c a*, *g a* and *g s* refer to classical-atomic, generic-atomic, and generic-slope-like indices, respectively.

Figure 4 shows the iso-probability contours for the dwarf and RGB PDFs, along with the position of the training set stars overlaid on the contours. Although there is some overlap in this diagnostic as well, there is clear differentiation between dwarf and RGB stars at $(V - I)_0$ colors redder than ~ 2 , with dwarf stars showing increasingly strong Na I absorption.

3.2.5. CMD Position

Position in the $(I, V - I)$ CMD provides yet another dwarf/RGB discriminator. The locii of RGB stars, spanning a wide range of metallicities and ages but all at the same distance from us, form a well-defined shape in the CMD as delineated by fiducial model RGB tracks (Fig. 11). By contrast, dwarf stars form a broad swath in color-magnitude space as they tend to be spread out over a wide range of line-of-sight distances. They also tend to have brighter I magnitudes. To pursue this as a diagnostic, we defined two parameters to describe a star’s position in the CMD: Y_{CMD} is the distance of a star along an isochrone,

running from 0 at $I_0 = 22.5$ (limiting magnitude of our spectroscopic sample) to 1 at the tip of the RGB, and X_{CMD} is the distance of a star on a line drawn across the set of isochrones, running from 0 at the most metal-poor isochrone used in our analysis, $[\text{Fe}/\text{H}] = -2.3$, to 1 at the most metal-rich isochrone $[\text{Fe}/\text{H}] = +0.5$. The lines across the isochrones are drawn by connecting points of roughly equal mass bins. Values of $Y_{\text{CMD}} < 0$ denote stars fainter than $I_0 \sim 22.5$, and values of $Y_{\text{CMD}} > 1$ denote stars above the tip of the RGB (values for these stars are calculated by linear extrapolation of the isochrones). Likewise, values of $X_{\text{CMD}} < 0$ denote objects bluer than the most metal-poor isochrone, and values of $X_{\text{CMD}} > 1$ denote objects redder than the most metal-rich isochrone (calculated by non-linear extrapolation of the lines drawn through the isochrones). The grid of isochrones used in this analysis are from Vandenberg et al. (2006) and correspond to an age of $t = 12.6$ Gyr and $[\alpha/\text{Fe}] = 0$.

The distributions in X_{CMD} and Y_{CMD} are combined to make the final two-dimensional PDF. In the context of § 3.2.1 and Eqn. 3, setting x to Y_{CMD} and y to X_{CMD} (instead of vice versa) lends itself more naturally to our PDF construction scheme. Specifically, single Gaussians were fit to the Y_{CMD} distributions for the RGB and dwarf training sets. The stars were then divided into bins according to their Y_{CMD} values, and running Gaussian parameters were fit to the X_{CMD} distributions. For each of the RGB and dwarf star training sets, the fits to the Y_{CMD} and X_{CMD} distributions were multiplied to make the final two-dimensional PDF. Figure 5 shows the iso-probability contours for the PDFs and the dwarf and RGB training sets. There is a lot of overlap in this diagnostic, but there is still some differentiation between the two populations. Since the RGB stars follow the isochrones, they form a rectangular distribution in X_{CMD} and Y_{CMD} space. In contrast, the dwarfs are evenly distributed in the $(I, V - I)$ CMD, and since the metal-rich isochrones curve to redder colors, the X_{CMD} values of bright dwarf stars become progressively smaller with increasing Y_{CMD} values.

We have chosen to frame the CMD diagnostic in terms of $(X_{\text{CMD}}, Y_{\text{CMD}})$ instead of the purely observational parameters $(I, V - I)$. While the values of X_{CMD} and Y_{CMD} are model dependent, the *separation* between the RGB and dwarf PDFs is independent of the details of the theoretical RGB tracks used to compute X_{CMD} and Y_{CMD} . For example, changing the adopted age or $[\alpha/\text{Fe}]$ for the model isochrones would introduce a small change in the X_{CMD} (and $[\text{Fe}/\text{H}]_{\text{phot}}$) values but the change would be the same for RGB and dwarf stars at any given location in the CMD. Neither the separation between the RGB and dwarf PDFs nor their widths would be affected by such a change. The effectiveness of any diagnostic in isolating M31 RGB stars from MW dwarf stars depends on the separation between the two PDFs relative to their widths. The distribution of M31 RGB stars in $(X_{\text{CMD}}, Y_{\text{CMD}})$ space is more physically meaningful than their CMD distribution: for example, there is a one-to-one mapping from X_{CMD} to $[\text{Fe}/\text{H}]_{\text{phot}}$. Moreover, X_{CMD} and Y_{CMD} are independent of each other in the RGB PDF and this makes it particularly easy to construct the two-dimensional PDF

within this space.

3.2.6. Photometric versus Spectroscopic Metallicity Estimates

The photometric metallicities ([Fe/H] estimates) for our data set are based on the comparison of a star’s position in the (I , $V - I$) CMD with the above grid ($\Delta Z = 0.0001$) of RGB isochrones at the distance of M31 (Vandenberg et al. 2006). Since the photometric metallicity estimates are based on the assumption that the stars are red giants at the distance of M31, it is inherently incorrect for dwarf stars. Hence, we expect a clear separation between the photometric and spectroscopic [Fe/H] estimates for giants and dwarfs.

Spectroscopic estimates for [Fe/H] are based on measurement of the Ca II triplet at $\lambda \sim 8500$ Å. The EW of the Ca II triplet (ΣCa) was calculated using a linear combination of the EWs of the three lines that has been shown to maximize the S/N of the feature (Rutledge, Hesser, & Stetson 1997a):

$$\Sigma \text{Ca} = 0.5 \text{EW}(\lambda 8498 \text{ Å}) + 1.0 \text{EW}(\lambda 8542 \text{ Å}) + 0.6 \text{EW}(\lambda 8662 \text{ Å}). \quad (4)$$

The EW of the individual Ca II lines was measured in 18 Å wide bins. $[\text{Fe}/\text{H}]_{\text{spec}}$ was calculated from ΣCa using an empirical calibration relation: (Rutledge et al. 1997b):

$$[\text{Fe}/\text{H}]_{\text{spec}} = -2.66 + 0.42 [\Sigma \text{Ca} - 0.64(V_{\text{HB}} - V)]. \quad (5)$$

The last term in the equation, ($V_{\text{HB}} - V$), corrects for the effect of surface gravity based on the difference between the V band apparent magnitude and the apparent magnitude of M31’s horizontal branch ($V_{\text{HB}} = 25.17$) (Holland et al. 1996). This calibration relation is derived from RGB stars in MW globular clusters spanning a range of metallicities.

In the construction of the PDFs, x and y were set to $[\text{Fe}/\text{H}]_{\text{phot}}$ and $[\text{Fe}/\text{H}]_{\text{spec}}$, respectively (§ 3.2.1). Analytical fits were made to the dwarf and RGB training set $[\text{Fe}/\text{H}]_{\text{phot}}$ distributions. Each training set was then divided into $[\text{Fe}/\text{H}]_{\text{phot}}$ bins, and Gaussians were fit to the $[\text{Fe}/\text{H}]_{\text{spec}}$ distribution in each bin. A quadratic function was fit to the Gaussian parameters of each of the RGB and dwarf star training sets. The $[\text{Fe}/\text{H}]_{\text{spec}}$ distribution was constructed based on the running Gaussian parameters given by the quadratic fit. For each training set, the analytic fits to the $[\text{Fe}/\text{H}]_{\text{phot}}$ and $[\text{Fe}/\text{H}]_{\text{spec}}$ distributions were multiplied to make the final two-dimensional PDF. Figure 5 shows the PDF contours and training set distributions in $[\text{Fe}/\text{H}]_{\text{spec}}$ vs. $[\text{Fe}/\text{H}]_{\text{phot}}$. As expected, the M31 RGB stars lie close to the one-to-one relation while the dwarf stars are well removed from it; there is a clear difference between the RGB and dwarf populations.

In using the above calibration relation, we are implicitly assuming that RGB stars in M31 are similar to those in MW globular clusters in terms of having old ages and $[\alpha/\text{Fe}] \sim +0.3$. The latter is different from our value of $[\alpha/\text{Fe}] = 0$ adopted in deriving the $[\text{Fe}/\text{H}]_{\text{phot}}$ estimates for this diagnostic. In their study of M31’s extended bulge, Brown et al. (2003) find that in addition to the majority old population there is a significant intermediate-age (6–8 Gyr) population present. Any difference between our adopted parameters and the unknown age and α enhancement of M31’s halo RGB stars will cause our $[\text{Fe}/\text{H}]_{\text{phot}}$ and $[\text{Fe}/\text{H}]_{\text{spec}}$ estimates to be offset from their true values. However, as discussed in § 3.2.5, such offsets will not affect the effectiveness of the diagnostic. For a more detailed treatment of the M31 RGB metallicity estimates, we refer the reader to Kalirai et al. (2006a).

3.2.7. Other Diagnostics

In this section we discuss two diagnostics based on K I and three diagnostics based on TiO . These five diagnostics have a lot in common with the Na I diagnostic and with one another (§ 4.2.1). The three TiO diagnostics have a smaller separation between RGB and dwarf stars than the Na I or K I diagnostics. Our present method is set up for combining diagnostics that are independent of one another so we have decided to exclude the K I and TiO diagnostics from the overall likelihood scheme (§ 3.3). We include them in this section because planned improvements to our diagnostic method will enable us to incorporate them in the future (§ 4.3.1).

K I Equivalent Width—

The EWs of the K I absorption lines at 7665 and 7699 Å, like the EW of Na I , are dependent on temperature as well as surface gravity, making them potential dwarf/giant discriminators. The continuum bandpasses and main bandpasses used to measure the EWs of the K I absorption lines are listed in Table 3. The construction of the two-dimensional RGB and dwarf PDFs for each of the two K I lines followed exactly the same procedure as for the Na I line (§ 3.2.4).

The iso-probability contours and the RGB and dwarf training sets are shown in Figure 7. As in the Na I diagnostic, the M31 RGB and MW dwarf distributions overlap at bluer colors, but diverge at redder colors ($(V - I)_0 > 2.5$), with the strength of the K I absorption lines increasing with increasing $(V - I)_0$ for dwarf stars.

Strength of TiO Bands—

Absorption molecular bands are the strongest spectral features of cool stars. In particular, TiO bands are apparent in early M-type stars and their strength increases with decreasing temperature. For a given temperature, TiO bands of RGB stars are stronger than those of dwarf stars, making these spectral features useful dwarf/giant discriminators in the low temperature regime. A detailed explanation of the behaviour of TiO bands (e.g., those around $\lambda \sim 8500$ and 8900 Å) is provided in Cenarro et al. (2001, 2006) on the basis of an extensive, empirical stellar library in the near-infrared.

We have measured the TiO bands at $\lambda \sim 7100$, 7600 , and 8500 Å using the different index definitions listed in Table 3. TiO_{7100} is a classic atomic index for the TiO band at $\lambda \sim 7100$ Å that consists of two continuum bandpasses and one central bandpass. For the TiO band at $\lambda \sim 8500$ Å we have followed the generic¹² slope-like index definition of Cenarro et al. (2003). In short, the signal of pixels within five continuum bandpasses (see Table 3) are used to fit a straight line—a pseudo-continuum, $F_C(\lambda)$ —over the region dominated by the TiO bands. The TiO_{8500} index is thus computed as the ratio between the pseudo-continuum values at the central wavelengths of the reddest and bluest continuum bandpasses: $\text{TiO}_{8500} = F_C(\lambda 8784.0)/F_C(\lambda 8479.0)$. In a sense, it may be considered to be a measure of the local pseudo-continuum slope, so TiO_{8500} values around 1 mean that no TiO band is present in the spectra. Finally, the strength of the TiO band at $\lambda \sim 7600$ Å, TiO_{7600} , is defined to be the mean of three normalized, different index definitions: $\text{TiO}_{7600}(1)$, $\text{TiO}_{7600}(2)$, and $\text{TiO}_{7600}(3)$. $\text{TiO}_{7600}(1)$ and $\text{TiO}_{7600}(2)$ are classic atomic index definitions—the latter having a narrower central bandpass—whereas $\text{TiO}_{7600}(3) [= F_C(\lambda 7734.5)/F_C(\lambda 8099.5)]$ is another slope-like index defined by means of six continuum bandpasses (see Table 3). Since the spectra of our target stars are usually affected by inter-CCD gaps located around this spectral region, we preferred to employ different index definitions in order to ensure a large number of training set stars having available index measurements for this TiO band. Thus, in case any of the above index definitions was not reliable or impossible to measure, means of the remaining reliable measurements were computed to derive the final TiO_{7600} value.

Two-dimensional RGB and dwarf PDFs for each of the three TiO diagnostics were constructed following the same procedure as for the Na I line (§ 3.2.4). Figure 8 shows the iso-probability contours for the dwarf and RGB PDFs, along with the position of the training set stars overlaid on the contours. It is clear that TiO diagnostics are not really useful for $(V - I)_0$ colors $\lesssim 2.0$ (since no apparent TiO bands are found for those temperatures). However, the TiO strengths of dwarf and RGB stars follow two different increasing trends

¹²Generic indices, defined as those having multiple continuum and central bandpasses, are specially suited to measure spectral features in regions crowded by other contaminating features, sky emission line residuals, and telluric absorption.

with increasing $(V - I)_0$. Since TiO_{7600} might be affected by nearby telluric absorption, the discriminating power of this index is not as clear cut as it is for TiO_{7100} and TiO_{8500} .

3.3. Computation of Likelihood Values

For each star in our survey with a measured blueshift, the probability the star is a red giant (P_{giant}) or a dwarf (P_{dwarf}) is calculated based on the normalized RGB and dwarf star PDFs. The likelihood a star i is a red giant in a given diagnostic j is computed using the formula

$$L_{ij} = \log \left(\frac{P_{\text{giant}}}{P_{\text{dwarf}}} \right). \quad (6)$$

To determine a star's overall likelihood value, we compute a weighted average of all the individual likelihoods available for each star:

$$\langle L_i \rangle = \frac{\sum_j w_j L_{ij}}{\sum_j w_j}, \quad (7)$$

summed over the available diagnostics. In general, all available individual likelihoods for a given star receive equal weight, $w_j = 1$. The only exception to this is for stars that are outliers in *both* the RGB and dwarf PDFs in any of two-dimensional diagnostics ($\text{Na}\,\text{I EW}$, CMD position, and $[\text{Fe}/\text{H}]_{\text{phot}}$ vs. $[\text{Fe}/\text{H}]_{\text{spec}}$). For such stars the corresponding diagnostic is assigned a lower weight ($w_j < 1$) as described below. The purpose of this is to downweight, and in extreme cases effectively remove from the overall likelihood estimate, diagnostics in which the star lies in a region of parameter space that is poorly sampled by both the RGB and dwarf star training sets. For the same reason, the individual likelihoods are capped at ± 5 , which corresponds to a P_{giant} to P_{dwarf} ratio of 10^5 or 10^{-5} .

Specifically, this downweighting occurs for stars that satisfy the criteria: $P_{\text{giant}} < 3\sigma_{\text{giant}}$ and $P_{\text{dwarf}} < 3\sigma_{\text{dwarf}}$ in a given diagnostic, where the probability thresholds σ_{giant} and σ_{dwarf} represent the probability levels which include 90% of the RGB and dwarf training set stars, respectively. The weight w_j assigned to such a star in the j -th diagnostic is:

$$w_j = \frac{w_0}{\left(\frac{\sigma}{P}\right)_{\text{giant}}^2 + \left(\frac{\sigma}{P}\right)_{\text{dwarf}}^2}, \quad (8)$$

where w_0 is set to 2/9 to ensure that the weights are well-behaved for stars that are close to the above thresholds. We also investigated weighting the individual likelihoods for all stars

in all diagnostics based on the measurement errors in the relevant parameters (§ 2.3), but found no significant differences in the overall likelihood distributions.

We found that the addition of the K_1 and TiO diagnostics did not improve our ability to separate RGB and dwarf stars, and in fact hurt it by putting too much weight on $(V - I)_0$ colors. There is strong covariance among the Na_1 , K_1 , and TiO diagnostics because they share a common color axis (see § 4.2.1 for more details). The three TiO diagnostics are not as sensitive as the Na_1 diagnostic—the vertical separation between the dwarf and RGB PDFs in the TiO diagnostics is relatively small (Fig. 8)—and the degeneracy between the RGB and dwarf PDFs for hot stars in the K_1 diagnostics extends to redder colors than in the Na_1 diagnostic (compare Figs. 4 and 7). Furthermore, the fractional measurement error in the EW is larger for K_1 and TiO than for Na_1 : the K_1 lines and TiO_{7600} band are affected by the atmospheric A-band, and the two reddest TiO bands are occasionally affected by spectral continuum discontinuity artifacts at the inter-CCD interface in DEIMOS.

For these reasons we do *not* include the K_1 and TiO diagnostics in our final calculation of the overall likelihood. We have nevertheless decided to present the details of the five K_1 and TiO diagnostics as they may be useful for other data sets. Moreover, in § 4.3.1 we discuss future modifications that should render the Na_1 , K_1 , and TiO diagnostics independent of one another.

3.4. Overall Likelihood Distributions

Figure 9 shows the distribution of overall likelihood values for each of our Keck/DEIMOS fields. These histograms use all available diagnostics (excluding K_1 and TiO) for each star.

The overall likelihood distributions for each field were used to determine whether a star was a red giant or a dwarf. The overall likelihood ($\langle L_i \rangle$) histograms in Figure 9 show obvious peaks at $\gtrsim +1$ (RGB) and $\lesssim +1$ (dwarf). The relative height of the peaks change with radius: in fields with approximately equal numbers of RGB and dwarf stars we see a clear bimodality (ie. field a13), while for inner fields we see a strong peak of RGB stars with a tail of dwarf stars, and vice versa for the outer fields. Stars with $\langle L_i \rangle > 0$ are designated M31 RGB stars, and stars with $\langle L_i \rangle < 0$ are designated foreground MW dwarf stars.

Figure 10 illustrates the power of our RGB/dwarf separation technique using stars in the $R = 30$ kpc minor-axis field a0. The individual likelihoods—defined as $L_j \equiv (P_{\text{giant}}/P_{\text{dwarf}})$ for the j -th diagnostic—for the five primary diagnostics are plotted against one another (L_j vs. L_k). Histograms for each individual likelihood L_j are plotted in the panels along the lower-right diagonal. It is encouraging to see that stars that are classified as M31 RGB stars

by our likelihood-based method (blue points) tend to lie in the top right quadrant of all panels ($L_j, L_k > 0$) while those classified as MW dwarf stars (red points) tend to lie in the bottom left quadrant ($L_j, L_k < 0$). No single diagnostic is able to discriminate perfectly between M31 RGB and MW dwarf stars, however the combination of diagnostics is very effective at separating the two stellar types.

Although there is no explicit weighting of the diagnostics (§ 3.3), some are more powerful than others. Diagnostics with a large separation between the RGB and dwarf PDFs (relative to the widths of the PDFs) will have a large range of individual likelihood values and vice versa (e.g., compare the range of L_v vs. L_{CMD} values in Fig. 10). Thus, diagnostics with a small separation between the dwarf and RGB PDFs will implicitly have less of an effect on the overall likelihood value.

The overall range of L_{CMD} and L_{DDO51} is small with respect to the other diagnostics. This is because of the substantial overlap between the RGB and dwarf PDFs for these two diagnostics. Despite the small range, there appears to be a fairly clear RGB/dwarf separation in both of these diagnostics, indicating that our measurement error in these quantities is small compared to the width of the corresponding distribution. In field a0 the $L_{\text{Fe/H}}$ diagnostic appears to be the least discriminatory of all the diagnostics. This is because of instrumental/data reduction problems with our early DEIMOS spectra (most of our a0 spectra are from fall 2004). The Ca II triplet in particular is severely affected by sky subtraction errors in the a0 spectra. By contrast the Na I doublet is in a part of the spectrum free of strong night sky emission lines and is well removed from the DEIMOS inter-CCD gap so the L_{Na} diagnostic is well behaved in field a0. Despite its relative poor performance in field a0, the $L_{\text{Fe/H}}$ diagnostic in general works better than the CMD diagnostic and as well as the DDO51 diagnostic.

We next attempt to quantify how each individual diagnostic performs on the secure samples of M31 RGB stars and MW dwarf stars (Class +3/+2 and –3/–2, respectively; see § 3.5). Depending on whether the individual likelihood value for the j -th diagnostic and i -th secure M31 RGB star [as defined by Eqn. (6)] is $> +0.5$, between -0.5 and $+0.5$, or < -0.5 , that star is deemed to have a correct, uncertain, or incorrect classification. Similar classifications are attempted for secure MW dwarf stars using individual diagnostics. The percentages of correct, uncertain, and incorrect classifications are listed in Table 4 for each of the five primary diagnostics using secure RGB/dwarf stars in two broad radial bins: $R = 30$ – 60 kpc (fields a0, a3, and a13) and $R = 60$ – 165 kpc (fields a19, m6, b15, m8, and m11). The radial velocity diagnostic is the most effective (highest percentage of correct classifications; the lowest percentage of uncertain/incorrect classifications) while the CMD diagnostic is the least effective. The Na I EW diagnostic is the second best; the DDO51 and $[\text{Fe}/\text{H}]_{\text{phot}}$ vs.

Table 4: Comparing the effectiveness of the five primary diagnostics.^a

Diagnostic(s)	$R = 30\text{--}60 \text{ kpc}$						$R = 60\text{--}165 \text{ kpc}$					
	Secure RGB (142)			Secure Dwarf (70)			Secure RGB (22)			Secure Dwarf (202)		
	Corr.	Unc.	Inc.	Corr.	Unc.	Inc.	Corr.	Unc.	Inc.	Corr.	Unc.	Inc.
L_v	96.5	2.8	0.7	85.7	11.4	2.9	90.9	4.5	4.5	92.6	5.0	2.5
L_{DDO51}	70.4	26.1	3.5	64.3	20.0	15.7	68.2	27.3	4.5	73.3	20.3	6.4
L_{Na}	80.3	16.9	2.8	68.6	25.7	5.7	77.3	22.7	0.0	71.3	21.3	7.4
L_{CMD}	44.4	54.9	0.7	21.4	72.9	5.7	63.6	36.4	0.0	24.8	73.3	2.0
$L_{\text{Fe/H}}$	66.2	23.9	9.9	85.7	11.4	2.9	54.5	27.3	18.2	79.2	17.8	3.0
$\langle L \rangle_2^b$	94.4	4.9	0.7	84.3	14.3	1.4	90.9	9.1	0.0	90.1	7.4	2.5
$\langle L \rangle_3^c$	95.8	4.2	0.0	94.3	4.3	1.4	90.9	9.1	0.0	95.5	3.0	1.5
$\langle L \rangle_4^d$	100.0	0.0	0.0	94.3	4.3	1.4	100.0	0.0	0.0	96.5	2.0	1.5

^aPercentage of secure RGB/dwarf stars in a given radial bin that were correctly classified by a given diagnostic/combination of diagnostics (“Corr.”), had an uncertain classification (“Unc.”), or were incorrectly classified (“Inc.”); see text for details. Secure RGB stars are defined to be Class +3 and +2 stars while secure dwarf stars are defined to be Class −3 and −2 stars (see § 3.5 and Table 5); the total number in each radial bin is given in parentheses after the column headings.

^bWeighted average of the two best diagnostics: L_v and L_{Na} .

^cWeighted average of the three best diagnostics: L_v , L_{Na} , and L_{DDO51} .

^dWeighted average of the four best diagnostics: L_v , L_{Na} , L_{DDO51} , and $L_{\text{Fe/H}}$.

[Fe/H]_{spec} diagnostics are comparable. Weighted averages of various subsets of diagnostics are also tested; their percentages are listed next in Table 4.

3.5. Subclassification of the Red Giant and Dwarf Star Samples

In general, stars with $\langle L_i \rangle > 0$ are M31 RGB stars while those with $\langle L_i \rangle < 0$ are foreground MW dwarf stars. We have developed a classification scheme which divides each of the RGB and dwarf samples into three classes, with Class +3 (−3) being the most secure and Class +1 (−1) the least secure. The classes are based primarily on $\langle L_i \rangle$, but X_{CMD} is used as a secondary criterion (§ 3.2.5). The most secure RGB (Class +3) and dwarf stars (Class −3) are identified as those with $\langle L_i \rangle > 0.5$ and $\langle L_i \rangle < -0.5$, respectively. However, to be classified as a Class +3 object, a star must also pass the $X_{\text{CMD}} \geq 0.0$ criterion, which

ensures that it falls within the color range of theoretical RGB isochrones at the distance of M31.

Stars with $\langle L_i \rangle > 0.5$ and $-0.05 \leq X_{\text{CMD}} < 0$ are designated Class +2. The errors in our X_{CMD} measurement are approximately 0.05 (the errors are a little larger than this at the faint end of our sample and smaller at the bright end). Thus, Class +2 stars are those with large $\langle L_i \rangle$ values that lie slightly bluer than (but roughly consistent with) the most metal-poor isochrone.

Table 5: Confirmed M31 RGB and MW dwarf stars for each of the fields.^a

Field	R (kpc)	No. Sci. Spectra ^b	No. M31 RGB Stars			No. MW Dwarf Stars			Comments
			Class +3	Class +2	Class +1	Class -3	Class -2	Class -1	
H11	12	234	102	0	13	17	1	6	
H13s	21	221	83	1	20	18	1	6	giant southern stream field
H13d ^c	25	136	67	19	disk field
a0	30	245	61	4	10	30	2	3	
a3	33	224	59	0	8	13	0	4	giant southern stream field
a13	60	141	16	2	2	23	2	3	
a19	81	68	4	0	2	23	0	3	
m6	87	138	7	2	0	44	3	8	
b15	95	127	5	0	2	24	1	10	
m8	121	109	1	0	2	22	2	5	
m11	165	283	3	0	4	82	1	11	

^aThe subclassification of the M31 RGB stars into Class +3, +2, and +1 and MW dwarf stars into Class -3, -2, and -1 (very secure, secure, and marginal) is discussed in § 3.5.

^bNumber of unique science spectra, excluding duplicate measurements (§ 2.3), $Q = -2$ instrumental failures (§ 2.2), and alignment stars.

^cThe photometry in our H13d field is currently undergoing recalibration so we do not attempt to subclassify the M31 RGB stars and MW dwarf stars at this point.

The least secure/marginal M31 RGB stars (Class +1) are defined to be those with $0.0 < \langle L_i \rangle \leq 0.5$ and $X_{\text{CMD}} \geq -0.05$. Likewise, the marginal MW dwarf stars (Class -1) are those with $-0.5 \geq \langle L_i \rangle \leq 0.0$ and $X_{\text{CMD}} \geq -0.05$. We expect some misclassification of stars within the range $-0.5 \leq \langle L_i \rangle \leq 0.5$, because stars with $\langle L_i \rangle$ values in this range often

have a spread of individual likelihood values, some positive (they follow the RGB PDF) and some negative (they follow the dwarf PDF).

Finally, stars with $\langle L_i \rangle \geq -0.5$ and $X_{\text{CMD}} < -0.05$ are designated Class -2 objects. These objects fall considerably blueward of the most metal-poor theoretical isochrone in the CMD. We disregard the $\langle L_i \rangle$ values of these stars because the diagnostic method does not work well for such blue objects (§§ 4.1.2–4.1.3).

This classification scheme allows us to systematically identify marginal stars and remove them from our analysis. Table 5 lists the number of M31 RGB and MW dwarf stars per class in each field. Figure 11 (*top and middle*) shows the distribution in the CMD of the three RGB classes and three dwarf classes, respectively.

4. Discussion of the Method

4.1. Statistical Tests

4.1.1. Evidence of M31 RGB Stars in the Outermost Fields

Is it possible that the stars identified as secure M31 RGB stars in our outermost fields are actually misidentified MW dwarf stars (e.g., stars in tails/outskirts of the dwarf star distributions in the various diagnostic parameter spaces)? We do not know *a priori* what fraction of the overall dwarf population is in the form of such outliers, but expect the fraction to be the same in all fields. By contrast, the ratio of secure RGB stars to secure MW dwarfs is observed to decline monotonically with increasing projected distance from M31’s center (Guhathakurta et al. 2005).

Given the very small number of secure M31 RGB stars found in our outermost halo fields, it is very important to check whether the properties of these stars are similar to those of the bulk of M31 RGB stars in our sample. Figure 12 compares the distribution of very secure M31 RGB (Class $+3$) stars in our two outermost fields m8 and m11 to that of foreground MW dwarf stars in four of the diagnostic plots. The handful of very secure M31 RGB stars and the far more numerous secure M31 dwarf stars follow the RGB and dwarf PDFs, respectively. This suggests that the Class $+3$ objects found in these fields are indeed genuine M31 RGB stars.

Figure 13 shows the $(V - I)_0$ color distribution of secure+marginal M31 RGB (Class > 0) and secure+marginal MW dwarf (Class < 0) stars. The color distribution of the M31 RGB stars peaks at $(V - I)_0 \sim 1.5$ with a tail to redder colors. The MW dwarf stars have

a bimodal distribution, with a peak at $(V - I)_0 \sim 2.3$ and a smaller peak at $(V - I)_0 \sim 1$. We fit the color distribution of stars in each of three radial bins as a linear combination of the RGB and dwarf color distributions: the $R = 30\text{--}85$ kpc, $R = 85\text{--}125$ kpc, and $R = 165$ kpc (m11) samples are best fit by 75%/25%, 45%/55%, and 5%/95% RGB/dwarf combinations, respectively. Stars in our furthest halo field m11 closely follow the MW dwarf color distribution, except for a slight bump at $(V - I)_0 \sim 1.5$. Such a bump is not present in the dwarf color distribution, but the M31 RGB color distribution has a peak at about this color. This bump in the m11 color distribution is where the Class +3 and all but one of the Class +1 stars are located. The colors of these objects suggest that they are in fact M31 RGB stars.

4.1.2. *Nature of the Bluest Stars (Class ± 2)*

There are 49 stars in our sample with $X_{\text{CMD}} < 0$ (i.e., bluer than the most metal-poor isochrone, $(V - I)_0 \lesssim 1$). The Na i , K i , and TiO diagnostics have no discriminating power for such blue stars. Also, these stars lie in the remote outskirts of both RGB and dwarf PDFs in the CMD and [Fe/H] diagnostics; the downweighting of outliers in the overall likelihood calculation ensures that these two diagnostics carry little weight. This leaves only two out of the five diagnostics, L_v and L_{DDO51} . As a further complication, some of the bluest MW dwarfs in our sample also have very negative velocities that overlap the distribution of M31 RGB stars (see § 4.2.3 and Fig. 18). For these reasons, we have taken a close look at these blue stars.

Metal-poor isochrones crowd together in the CMD—e.g., an isochrone with $[\text{Fe}/\text{H}] = -3$ is only slightly bluer than the bluest ($[\text{Fe}/\text{H}] = -2.3$) isochrone in Figure 11 (Vandenberg et al. 2006). Thus any star that lies well to the blue of our most metal-poor isochrone is almost certainly a MW dwarf star. A comparison of the $(V - I)_0$ color distributions of RGB and dwarf stars (thin histograms in middle panel of Fig. 13) confirms that stars with $(V - I)_0 \lesssim 1$ are $\approx 10\times$ more likely to be MW dwarfs than M31 RGB stars. This is reinforced in Figures 7 and 8: the dwarf PDF contours based on the final training set extend to $(V - I)_0 \lesssim 1$ whereas the RGB contours cut off sharply at $(V - I)_0 \sim 1$.

Of the 49 blue stars, 26 have overall likelihood $\langle L_i \rangle < -0.5$ and we feel confident in designating them Class -3 (very secure MW dwarf stars). Eleven of the 49 have overall likelihood $\langle L_i \rangle > -0.5$ but are significantly bluer than the most metal-poor isochrone ($X_{\text{CMD}} < -0.05$); we designate them Class -2 (secure MW dwarf stars). There are another 11 stars with overall likelihood $\langle L_i \rangle > +0.5$ that lie slightly blueward of the most metal-poor isochrone ($0.05 \leq X_{\text{CMD}} < 0$); they are designated Class $+2$ (secure M31 RGB stars). The

full set of classification criteria are given in § 3.5.

Figure 14 shows the distribution of Class +2 and –2 stars in the velocity and DDO51 diagnostic plots. The distribution of Class +2 stars in both diagnostics indicates that they are far more likely to be drawn from the RGB PDF than the dwarf PDF. The case for the Class –2 stars is more complicated. Their DDO51 parameters span a broad range [Fig. 14(d)], but this is to be expected: the locus of blue ($(V - I)_0 \lesssim 1$) dwarf stars lies close to the RGB selection box in the $(M - DDO51)$ vs. $(M - T_2)$ color-color plot (see Fig. 5 of Palma et al. 2003) so they are sometimes assigned a large DDO51 parameter value. The velocities of Class –2 stars are in the overlap region of the RGB/dwarf PDFs [Fig. 14(c)]. The Galactic star count model (Bahcall & Soneira 1984; Ratnatunga & Bahcall 1985) predicts that the radial velocity distribution of blue MW dwarf stars in our sample should be skewed toward negative values compared to that of faint red MW dwarfs (see Fig. 8 of Reitzel & Guhathakurta 2002). This is because MW dwarfs with $(V - I)_0 \lesssim 1$ must be main-sequence turnoff stars in the MW halo at heliocentric distances of 15–50 kpc (absolute mag: $(M_I)^{MSTO} \sim 4.0$; apparent mag range of our sample: $20 \leq I_0 \leq 22.5$). Members of the hot, non-rotating MW halo are expected to span a broad range of radial velocities centered on -175 km s^{-1} (reflex of solar motion in the direction of M31— Reitzel & Guhathakurta 2002), consistent with the observed distribution of Class –2 stars.

Even though Class +2 and –2 stars fall far outside the RGB and dwarf PDFs in the $[\text{Fe}/\text{H}]$ diagnostic, it is instructive to compare their $[\text{Fe}/\text{H}]_{\text{phot}}$ and $[\text{Fe}/\text{H}]_{\text{spec}}$ values. Class +2 stars have median $[\text{Fe}/\text{H}]_{\text{phot}}$ and $[\text{Fe}/\text{H}]_{\text{spec}}$ of –2.5 and –1.9, respectively, which are in reasonable agreement given the large measurement errors for metal-poor stars. By contrast, Class –2 stars have median $[\text{Fe}/\text{H}]_{\text{phot}}$ and $[\text{Fe}/\text{H}]_{\text{spec}}$ of $\lesssim -4$ and –2.0, respectively (the $[\text{Fe}/\text{H}]_{\text{phot}}$ estimates are admittedly based on gross extrapolation).

In conclusion, the velocities, DDO51 parameters, and (with greater uncertainty) $[\text{Fe}/\text{H}]$ estimates of the Class +2 and –2 stars are consistent with their designations as secure M31 RGB and MW dwarf stars, respectively.

4.1.3. *Nature of the Marginal Cases (Class ±1)*

The $\langle L_i \rangle$ distributions of RGB and dwarf stars are broad (Fig. 9): it is likely that some legitimate M31 RGB stars have scattered to negative $\langle L_i \rangle$ values, and some legitimate MW dwarf stars have scattered to positive $\langle L_i \rangle$ values. For this reason stars with $|\langle L_i \rangle| < 0.5$ are designated Class +1 or –1 (marginal RGB or dwarf stars; § 3.5).

If the shapes of the RGB and dwarf $\langle L_i \rangle$ distributions are the same from field to field,

the number of marginal RGB stars (Class +1) in a given field can be expressed as the sum of a fraction a of the number of secure RGB stars (Class +3 and +2) and a fraction b of the number of secure dwarf stars (Class –3 and –2) in that field:

$$N(\text{Class } +1) = a [N(\text{Class } +3) + N(\text{Class } +2)] + b [N(\text{Class } -3) + N(\text{Class } -2)]. \quad (9)$$

Similarly the number of marginal dwarf stars (Class –1) can be expressed as:

$$N(\text{Class } -1) = c [N(\text{Class } +3) + N(\text{Class } +2)] + d [N(\text{Class } -3) + N(\text{Class } -2)]. \quad (10)$$

Figure 15 (*top*) shows the ratio of marginal M31 RGB (Class +1) stars to secure RGB and dwarf stars (Class +3, +2, –3, and –2) as a function of the ratio of secure RGB to dwarf stars. Each data point represents one of our fields and the abscissa values are roughly in order of decreasing projected radial distance of the field from the center of M31. The data are consistent with $a = 0.07$ and $b = 0.03$ (solid line) but can also be fit by $a = b = 0.05$ (dashed horizontal line). The marginal dwarf (Class –1) stars are well fit by $c = 0.03$ and $d = 0.15$ [solid line in Fig. 15 (*bottom*)].

Based on the first pair of (a, b) values, about 75% of the stars in our overall Class +1 sample are expected to be true M31 RGB stars while the remaining 25% are expected to be MW dwarf stars. The mix of Class –1 stars is expected to be 80% MW dwarfs and 20% M31 RGB stars. These percentages apply to our *overall* samples of marginal stars; the mix varies from field to field of course.

Figure 16 shows the distribution of marginal M31 RGB (Class +1) stars in four of our five primary diagnostic plots (all except the CMD diagnostic). These stars have radial velocities in the region of overlap between the RGB and dwarf PDFs, a large spread of DDO51 values, and $(V - I)_0$ colors mostly in the range 1–2.5 which places them in the region of overlap of the RGB and dwarf PDFs in the Na i diagnostic plot—all consistent with their marginal overall likelihood value. The distribution of these stars in the [Fe/H] diagnostic plot is consistent with most being M31 RGB stars.

Figure 17 shows the distribution of marginal MW dwarf (Class –1) stars in the same four diagnostic plots. Their $(V - I)_0$ colors are mostly in the range 1–2, as for the Class +1 cases. The Na i diagnostic plot is not conclusive but the radial velocity, DDO51, and [Fe/H] diagnostic plots favor the MW dwarf designation.

In summary, the Class ± 1 stars are not as blue as the Class ± 2 stars, but most of the arguments about the performance of our method on blue stars applies here as well, only to a lesser degree (§ 4.1.2). The statistical analysis presented above [Fig. 15; Eqns. (9–10)] indicates that most of the Class +1 objects should be M31 RGB stars and most of

the Class –1 objects should be MW dwarf stars. The distribution in the diagnostic plots support this hypothesis.

4.2. Covariance among Diagnostics

4.2.1. *Na, K, and TiO*

The NaI , KI and TiO diagnostics (Figs. 4, 7, and 8) are clearly not independent; not only do they share a common color axis, but a star’s NaI , KI and TiO line strengths all depend on both temperature (color) and surface gravity. The degeneracy between the dwarf and RGB PDFs in these diagnostics at bluer $(V - I)_0$ colors (especially in KI and TiO) results in much of their discriminating power coming from the color distribution. Therefore, if most of the stars in the sample are bluer than $(V - I)_0 \sim 2.5$, the inclusion of all five of these diagnostics (NaI , two KI , and three TiO) will overly weight the color distribution in determining overall likelihood values. We choose to use only the NaI diagnostic, since it has the most discriminating power of the five. However, the KI and TiO diagnostics do have some discriminating power (beyond the color distribution) for redder stars, and could be used in an appropriate sample. Finally, although the two KI diagnostics are obviously not independent of each other (nor are the three TiO diagnostics), combining the two KI and three TiO diagnostics is beneficial since this will reduce the scatter caused by individual line strength measurement errors.

4.2.2. *Na, CMD, and [Fe/H]*

Although the vertical axes of the NaI , CMD, and $[\text{Fe}/\text{H}]$ diagnostics (Figs. 4, 5, and 6) are independent of each other, there is a complicated dependence between the horizontal axes of these three diagnostics. The horizontal axis of the NaI diagnostic is $(V - I)_0$ color. Both the horizontal axes of the CMD and $[\text{Fe}/\text{H}]$ diagnostics are dependent on color: X_{CMD} depends on position within the CMD with relation to the theoretical RGB isochrones (§ 3.2.5), as does $[\text{Fe}/\text{H}]_{\text{phot}}$ (§ 3.2.6). However, the dwarf and RGB PDFs in both the CMD and $[\text{Fe}/\text{H}]$ diagnostics cover the same horizontal range. All the discriminating power in these two diagnostics comes from the vertical axes, which are independent.

4.2.3. Correlations within the Dwarf Star Sample

We have explored all secure M31 dwarf stars for possible correlations between radial velocity and $(V - I)_0$ color and/or DDO51 parameter (Fig. 18). Most dwarf stars have small DDO51 parameters, as expected. Moreover, regardless of radial velocity, there is a tail to the distribution of DDO51 parameters reaching all the way up to values near unity. No strong trend is seen between radial velocity and $(V - I)_0$ color either. The few dwarf stars with very negative radial velocities ($v_{\text{hel}} < -225 \text{ km s}^{-1}$) are all very blue. However, the rest of the dwarf stars display a wide range of $(V - I)_0$ colors and show no correlation between radial velocity and color.

To ensure that the stars we have identified as secure M31 RGB stars are not simply the tail of the dwarf distribution in the outermost, sparsest M31 halo fields, we explored the dwarf training set for correlations between the positions of stars in the diagnostics. If a star in the tail of the dwarf distribution in one diagnostic is also in the tail of the dwarf distribution in the other diagnostics, it will receive a low probability of being a dwarf star in all of them, adding up to an spuriously high probability of being an RGB star. For four of the most powerful diagnostics (radial velocity, $\text{Na}\,\text{\scriptsize I}$ EW vs. $(V - I)_0$ color, DDO51 parameter, and $[\text{Fe}/\text{H}]_{\text{phot}}$ vs. $[\text{Fe}/\text{H}]_{\text{spec}}$), we chose dwarf training set stars in the tail of the dwarf distribution and investigated where they fell in the other three diagnostics. Figure 19 shows where stars selected to be in the tail of the dwarf distribution in the $\text{Na}\,\text{\scriptsize I}$ diagnostic ($(V - I)_0 < 2$) fall in the other diagnostics. It is clear that they do not fall in the tail of the dwarf distribution in radial velocity, DDO51 parameter, or in $[\text{Fe}/\text{H}]_{\text{spec}}$ vs. $[\text{Fe}/\text{H}]_{\text{phot}}$. The only correlation is a slight shift to lower $[\text{Fe}/\text{H}]_{\text{phot}}$ values. This is expected, since $[\text{Fe}/\text{H}]_{\text{phot}}$ is related to $(V - I)_0$ color. The tails of the dwarf distribution in the other diagnostics show the same behavior as in this example: no correlation was found between diagnostics.

4.3. Shortcomings of the Present Method and Future Improvements

While our likelihood-based RGB/dwarf separation method is vastly superior to the radial velocity cut used in other spectroscopic surveys of M31 stars (§ 4.4), it is far from optimal and will no doubt undergo improvements in the not-too-distant future. These improvements are beyond the scope of the present paper and will be tackled in a future paper; we list them here for the sake of completeness.

4.3.1. *Color Dependence of the Diagnostics*

The covariance of the diagnostics has been discussed in § 4.2. The degeneracy between the horizontal axes (color-dependence) of the two-dimensional diagnostics can be lifted by converting them to one-dimensional diagnostics. One method which holds promise for the future is to fit a spline to the distribution of training set stars in each diagnostic. The distribution of vertical distances of the training set stars from the fit will yield a one-dimensional PDF. Once a two-dimensional diagnostic is collapsed into a one-dimensional diagnostic in this way, the latter will have no sensitivity to differences in the $(V - I)_0$ color distribution between M31 RGB and MW dwarf star populations. This will enable us to incorporate the K₁ and TiO diagnostics into the overall likelihood.

4.3.2. *M31’s Radial Metallicity Gradient*

Another future improvement to the method will be to account for radial trends in the M31 RGB star properties. We are currently using one M31 RGB training set for all of our fields. However, we have discovered that M31 RGB stars at large radial distances are systematically more metal-poor than those at smaller radial distances (Kalirai et al. 2006a). Our present method is sub-optimal in that our RGB PDFs do not track the change in the $(V - I)_0$ color distribution of M31 stars with radial distance and are based on a training set that is drawn mostly from M31’s inner spheroid. In order to track this radial trend, we will need a significantly larger sample of RGB stars in M31’s outer halo to use as a training set. We expect that a much larger outer halo RGB sample will be available in the next few years.

4.3.3. *Accounting for Measurement Error and Eliminating Analytic PDFs*

The likelihood-based method developed in this paper does not explicitly take advantage of our (admittedly rough) knowledge of the measurement errors in the quantities used in our various diagnostic plots (§ 2.3). For idealized error distributions, each training set star can be treated as a Gaussian whose width is the quadrature sum of its own measurement error and that of the star for which the likelihood estimate is being made. Naturally, these would be one-dimensional Gaussians for the radial velocity and DDO51 diagnostics and two-dimensional Gaussians for the Na₁, CMD, and [Fe/H] diagnostics. The integral under the Gaussian would be the same for each training set star. The M31 RGB and MW dwarf PDFs would then be the sum of all the Gaussians corresponding to the training set stars. The integral under each PDF would be set to unity. We hope to implement such a procedure

in the future; with enough stars in the training set the sum of all the Gaussians should be smooth enough that it will no longer be necessary to fit analytic functions in order to derive PDFs.

4.3.4. *Estimating the Number of M31 RGB Stars*

Through most of this paper we have focused on the question: Which stars are M31 RGB stars and which ones are MW dwarf stars? Alternatively, one might ask: What is our best statistical estimate of the number of M31 RGB stars and MW dwarf stars in the sample? The first question is clearly important for addressing a wide variety of scientific topics (such as the metallicity or dynamics of a clean sample of M31 RGB stars), but the second question is more relevant when it comes to studies of the spatial density distribution of RGB stars and surface brightness profile and M31’s halo.

The distinction between the above two questions can be illustrated by the following simple scenario. Let us assume there is a measurable x and that M31 RGB stars and MW dwarf stars are characterized by different, but overlapping x distributions. Armed with only this information, it is impossible to assign a clear designation to any star whose x value lies in the overlap region. However, if the *shape* of underlying parent x distribution is known for M31 RGB and MW dwarf stars, one can fit a weighted sum of the RGB and dwarf star parent distributions to the observed x distribution and thereby determine the fraction of each stellar type in the sample.

In the context of our method, the RGB and dwarf PDFs for each diagnostic (modulo the other planned improvements of course) can be treated as the underlying parent distributions. One could then fit, simultaneously for all diagnostics, a weighted sum of the PDFs to the observed distribution of points. The outcome of the fit would be our best estimate for the M31 RGB fraction in each field. We plan to explore such a method in a future paper.

4.4. The Diagnostic Method Versus a Radial Velocity Cut

We assess the performance of the likelihood-based method presented in this paper by comparing it to the use of a simple radial velocity cut to select M31 RGB stars. Most previous spectroscopic studies of M31 RGB stars have resorted to using radial velocity cuts: for example, Reitzel & Guhathakurta (2002) used $v < -220$ km s $^{-1}$ while Ibata et al. (2005) used $v < -100$ km s $^{-1}$.

To investigate the improvement in M31 RGB sample size gained through using our

diagnostic method, we applied a velocity cut of $v < -220 \text{ km s}^{-1}$ to our smooth spheroid sample. (The disk-dominated field H13d and the stream stars in fields H13s and a3 are excluded from this count.) This resulted in an RGB sample of 208 stars, compared to 207 stars identified by the likelihood method as secure (Class +3 and +2) RGB stars. However, only 192 stars are in common between the two samples. This velocity cut recovers 93% of the M31 RGB stars, and 8% of the velocity-selected RGB stars are actually MW dwarf star contaminants. If we restrict our analysis to the outer halo fields (fields a13 through m11), this velocity cut yields 42 stars while our likelihood method yields 40 secure RGB stars, with 36 stars in common. Thus, a velocity cut of $v < -220 \text{ km s}^{-1}$ in the outer halo recovers 90% of the M31 RGB stars in these fields, but suffers from a MW dwarf star contamination rate of 19%. As an extreme case, an $L_v > +0.5$ cut in the radial velocity diagnostic (which corresponds $v < -190 \text{ km s}^{-1}$) yields four stars in our outermost field m11 ($R = 165 \text{ kpc}$), but only two of these are secure M31 RGB stars, while one each is a secure MW dwarf and a marginal MW dwarf—i.e., a 50% contamination rate. Moreover, one of the secure M31 RGB stars in this field fails this velocity cut.

If a less conservative velocity cut is made, all the RGB stars can be recovered, but at the price of a larger dwarf contamination rate. When a velocity cut of $v < -100 \text{ km s}^{-1}$ is made in H11, our innermost smooth spheroid field, it yields 120 stars, while our likelihood method finds 102 secure RGB stars. The sample selected solely on the basis of this velocity cut would have a dwarf contamination rate of 15%. If this velocity cut is made in field a0 as well as H11, it yields 203 stars, versus 167 secure RGB stars, for a dwarf contamination rate of 17.7%. Finally, if a somewhat more conservative velocity cut of $v < -160 \text{ km s}^{-1}$ (as in Chapman et al. 2006) is made in the smooth halo fields beyond $R = 30 \text{ kpc}$ from the nucleus (a0, a13 through m11) the total number of stars selected is 140, compared to 105 secure RGB stars, for a dwarf contamination rate of 25%.

In conclusion, we find that the radial velocity cuts that have been used to isolate M31 RGB stars in other spectroscopic surveys (e.g., Reitzel & Guhathakurta 2002; Ibata et al. 2005; Chapman et al. 2006) yield samples that contain a significant fraction of foreground MW dwarf star contaminants and/or are incomplete. While this may be acceptable for statistical studies of the inner regions of M31 where the surface density of RGB stars greatly exceeds that of foreground MW dwarf stars, the dwarf contamination presents a serious obstacle for studies of M31’s sparse outer halo. As discussed above, using a conservative radial velocity cut (say -200 km s^{-1}) reduces the dwarf contamination rate but causes other complications. For example, any dynamical analysis of a radial velocity-selected sample of RGB stars would have to take the cut into account. Given the large spread of M31 RGB radial velocities around $v_{\text{sys}}^{\text{M31}} = -300 \text{ km s}^{-1}$ (in its dynamically hot bulge and halo and fast rotating disk), a radial velocity cut of -200 km s^{-1} would lead to substantial

incompleteness/bias. By contrast, our likelihood-based method produces a clean unbiased sample of M31 RGB stars that can directly be used for dynamical (and other) studies.

4.5. Comparison to Photometric Studies

In this section we switch our attention from comparison with other spectroscopic studies to comparisons with photometric studies of the surface brightness profile of M31. It has long been recognized that star count studies are far superior to integrated light measurements (Pritchett & van den Bergh 1987, 1988, 1994). Star count studies typically select M31 RGB candidates based on location within the CMD and use control fields for statistical subtraction of the “background” (i.e., foreground MW dwarf star and background field galaxy contaminants—Pritchett & van den Bergh 1994; Durrell et al. 2004; Irwin et al. 2005). However, systematic errors in background subtraction (e.g., due to photometric and/or seeing variations) limit these techniques to regions of M31 where the surface density of RGB stars is comparable to or greater than the background level ($\mu_V \approx 30 \text{ mag arcsec}^{-2}$).

A variety of photometric filtering techniques have been used to increase the contrast of M31 RGB stars with respect to contaminants. An example of this is the use of *UBRI* photometry to reject background galaxies (Reitzel, Guhathakurta, & Gould 1998). As discussed in § 2, Ostheimer (2002) used DDO51 photometry to select M31 RGB candidates. This technique reduces the surface brightness level of the background to $\mu_V \gtrsim 31 \text{ mag arcsec}^{-2}$ (Guhathakurta et al. 2005).

In contrast to the above methods, using a combination of photometric and spectroscopic diagnostics allows us to reliably pick out very sparse groups of M31 RGB stars by rejecting foreground MW dwarf star and background field galaxy contaminants. The three secure M31 RGB stars identified in our outermost field m11 constitute only a few percent of the overall sample of DDO51-selected RGB candidates in that field; the rest are MW dwarf stars or galaxies. We use the ratio of secure M31 RGB stars to secure MW dwarf stars, in conjunction with a Galactic model (Bahcall & Soneira 1984; Ratnatunga & Bahcall 1985), to estimate M31’s surface brightness profile (Guhathakurta et al. 2005). This allows us to map the outer halo of M31 down to an unprecedented surface brightness level of $\mu_V \sim 35 \text{ mag arcsec}^{-2}$. Kalirai et al. (2006a) study the metallicity distribution of M31 RGB stars isolated by our diagnostic method and find that the stellar halo is significantly more metal poor than the bulge; this is in contrast to findings from previous photometric studies of a metal-rich stellar “halo” in M31 (e.g., Durrell et al. 2004; Irwin et al. 2005).

5. Conclusion

As part of a large spectroscopic survey of the outer halo of M31, we have developed a method to isolate a clean sample of RGB stars in M31. This method uses five diagnostics to isolate RGB stars: radial velocity, DDO51 photometry, the EW of the Na₁ absorption feature, CMD position, and a comparison of spectroscopic vs. photometric [Fe/H] estimates. We also explored diagnostics based on the EWs of the K₇₆₆₅ and K₇₆₉₉ absorption features, and the strengths of the TiO bands at 7100, 7600, and 8500 Å. The first five diagnostics are more or less independent of one another; the K₁ Na₁, and TiO diagnostics all show a dependence on stellar effective temperature and are only effective for cool (red) stars. The overall likelihood based on a combination of diagnostics proves to be a much more powerful tool than any of the individual diagnostics alone.

The diagnostic method gives us the ability to confidently identify very sparse populations of M31 RGB stars, and has led to the discovery of stars as distant as $R \sim 165$ kpc (in projection) from the galaxy's center. This technique has allowed us to reach surface brightness levels of $\mu_V \approx 35$ mag arcsec⁻² and has enabled us to find an extended stellar halo in M31 that follows an $R^{-2.6}$ surface brightness profile out to $R \sim 165$ kpc (Guhathakurta et al. 2005). An investigation of the properties of these RGB stars shows that the stars become increasingly metal-poor with increasing distance from M31's center: beyond $R > 60$ kpc, the mean metallicity of our secure M31 RGB sample is found to be $\langle [\text{Fe}/\text{H}]_{\text{phot}} \rangle = -1.26 \pm 0.10$ (Kalirai et al. 2006a). In addition to identifying sparse populations, our method for isolating M31 RGB stars has the benefit of permitting detailed dynamical studies of the M31 halo, since the selection of stars does not depend on a radial velocity cut and the resulting RGB sample is therefore not kinematically biased. The application of the diagnostic method to our M31 halo survey provides an unprecedented level of sensitivity, allowing us to reliably study the extent, structure, and kinematics of the remote M31 halo.

We are grateful to Sandy Faber and the DEIMOS team for building an outstanding instrument and for extensive help and guidance during its first observing season. We thank Peter Stetson, Jim Hesser, and James Clem for help with the acquisition and reduction of CFHT/MegaCam images, Phil Choi, Alison Coil, Geroge Helou, Drew Phillips, and Greg Wirth for observing some DEIMOS masks on our behalf, Drew Phillips and Marla Geha for help with slitmask designs, Leo Girardi for providing an extensive grid of theoretical stellar isochrones, Ricardo Schiavon for expert advice on spectral features, Jeff Lewis, Bill Mason, and Matt Radovan for fabrication of slitmasks, and the DEEP2 team for allowing us use of the `spec1d/zspec` software. The `spec2d` data reduction pipeline for DEIMOS was developed at UC Berkeley with support from NSF grant AST-0071048. This project was supported

by an NSF Graduate Fellowship (K.M.G.), NSF grants AST-0307966 and AST-0507483 and NASA/STScI grants GO-10265.02 and GO-10134.02 (P.G., K.M.G., J.S.K., and C.L.), NSF grants AST-0307842 and AST-0307851, NASA/JPL contract 1228235, the David and Lucile Packard Foundation, and The F. H. Levinson Fund of the Peninsula Community Foundation (S.R.M., J.C.O., and R.J.P.), NSF grant AST-0307931 (R.M.R. and D.B.R.), and a UCM Fundación del Amo Fellowship (A.J.C.). J.S.K. is supported by NASA through Hubble Fellowship grant HF-01185.01-A, awarded by the Space Telescope Science Institute, which is operated by the Association of Universities for Research in Astronomy, Incorporated, under NASA contract NAS5-26555.

REFERENCES

Bahcall, J. N. & Soneira, R. M. ApJS, 55, 67

Bellazzini, M., Cacciari, C., Federici, L., Fusi Pecci, F., & Rich, R. M. 2003, A&A, 405, 867

Bertin, E., & Arnouts, S. 1996, A&AS, 117, 393

Braun, R. & de Thilker, D. A. 2004, A&A, 417, 421

Brown, T. M., Ferguson, H. C., Smith, E., Kimble, R. A., Sweigart, A. V., Renzini, A., Rich, R. M., & VandenBerg, D. A. 2003, ApJ, 592, L17

Brown, T. M., Smith, E., Guhathakurta, P., Rich, R. M., Ferguson, H. C., Renzini, A., Sweigart, A. V., & Kimble, R. A. 2006, ApJ, 636, L89

Bullock, J. S., & Johnston, K. V. 2005, ApJ, 635, 931

Bullock, J. S., Kravtsov, A. V., & Weinberg, D. H. 2001, ApJ, 548, 33

Cenarro, A. J., Cardiel, N., Gorgas, J., Peletier, R. F., Vazdekis, A., & Prada, F. 2001, MNRAS, 326, 959

Cenarro, A. J., Gorgas, J., Vazdekis, A., Cardiel, N., & Peletier, R. F. 2003, MNRAS, 339, L12

Cenarro, A. J., et al. 2006, in preparation

Chapman, S. C., Ibata, R., Lewis, G. F., Ferguson, A. M. N., Irwin, M., McConnachie, A., & Tanvir, N. 2006, ApJ, submitted (astro-ph/0602604)

Choi, P. I., Guhathakurta, P., & Johnston, K. V. 2002, AJ, 124, 310

de Vaucouleurs, G. 1958, *apj*, 128, 465

Durrell, P. R., Harris, W. E., & Pritchett, C. J. 2004, *AJ*, 121, 2557

Durrell, P. R., Harris, W. E., & Pritchett, C. J. 2004, *AJ*, 128, 260

Faber, S. M., et al. 2003, *Proc. SPIE*, 4841, 1657

Ferguson, A. M. N., Irwin, M. J., Ibata, R. A., Lewis, G. F., & Tanvir, N. R. 2002, *AJ*, 124, 1452

Font, A. S., Johnston, K. V., Guhathakurta, P., Majewski, S. R., & Rich, R. M. 2006, *AJ*, 131, 1436

Guhathakurta, P., Ostheimer, J. C., Gilbert, K. M., Rich, R. M., Majewski, S. R., Kalirai, J. S., Reitzel, D. B., & Patterson, R. J. 2005, arXiv preprint (astro-ph/0502366)

Guhathakurta, P., Rich, R. M., Reitzel, D. B., Cooper, M. C., Gilbert, K. M., Majewski, S. R., Ostheimer, J. C., Geha, M. C., Johnston, K. V., & Patterson, R. J. 2006, *AJ*, 131, 2497

Helmi, A., & White, S. D. M. 1999, *MNRAS*, 307, 495

Helmi, A., & de Zeeuw, T. 2000, *MNRAS*, 319, 657

Holland, S. 1998, *AJ*, 115, 1916

Holland, S., Fahlman, G. G., & Richer, H. B. 1996, *AJ*, 112, 1035

Ibata, R., Chapman, S., Ferguson, A. M. N., Irwin, M., Lewis, G., & McConnachie, A. 2004, *MNRAS*, 351, 117

Ibata, R., Chapman, S., Ferguson, A. M. N., Lewis, G., Irwin, M., & Tanvir, N. 2005, *ApJ*, 634, 287

Ibata, R. A., Gilmore, G., & Irwin, M. J. 1994, *Nature*, 370, 194

Ibata, R., Irwin, M. J., Ferguson, A. M. N., Lewis, G., & Tanvir, N. 2001, *Nature*, 412, 49

Irwin, M. J., Ferguson, A. M. N., Ibata, R. A., Lewis, G. F., & Tanvir, N. R. 2005, *ApJ*, 628, 105

Johnston, K. V. 1998, *ApJ*, 495, 297

Johnston, K. V., Hernquist, L., & Bolte, M. 1996, *ApJ*, 465, 278

Kalirai, J. S., Gilbert, K. M., Guhathakurta, P., Majewski, S. R., Ostheimer, J. C., Rich, R. M., Cooper, M. C., Reitzel, D. B., & Patterson, R. J. 2006a, *ApJ*, in press, (astro-ph/0605170)

Kalirai, J. S., Guhathakurta, P., Gilbert, K. M., Reitzel, D. B., Rich, R. M., Majewski, S. R., & Cooper, M. C. 2006b, *ApJ*, 641, 268

Kent, S. M. 1983, *ApJ*, 266, 562

Majewski, S. R., Ostheimer, J. C., Kunkel, W. E., & Patterson, R. J. 2000, *AJ*, 120, 2550

Majewski, S. R., Skrutskie, M. F., Weinberg, M. D., & Ostheimer, J. C. 2003, *ApJ*, 599, 1082

Mathewson, D. S., Cleary, M. N., & Murray, J. D. 1974, *ApJ*, 190, 291

Morrison, H. L., et al. 2000, *AJ*, 119, 2254-2273

Mould, J. & Kristian, J. 1986, *ApJ*, 316, 517

Newberg, H. J., et al. 2003, *ApJ*, 596, L191

Ostheimer, J. C. 2002, Ph.D. thesis, University of Virginia

Pritchett, C. J., & van den Bergh, S. 1987, *ApJ*, 316, 517

Pritchett, C. J., & van den Bergh, S. 1988, *ApJ*, 331, 135

Pritchett, C. J., & van den Bergh, S. 1994, *AJ*, 107, 1730

Palma, C., Majewski, S. R., Siegel, M. H., Patterson, R. J., Ostheimer, J. C., & Link, R. 2003, *AJ*, 125, 1352

Ratnatunga, K. U. & Bahcall, J. N. 1985, *ApJS*, 59, 63

Reitzel, D. B., & Guhathakurta, P. 2002, *AJ*, 124, 234

Reitzel, D. B., Guhathakurta, P., & Gould, A. 1998, *AJ*, 116, 707

Reitzel, D. B., Guhathakurta, P., & Rich, R. M. 2004, *AJ*, 127, 2133

Rich, R. M., Mighell, K. J., Freedman, W. L. & Neill, J. D. 1996, *AJ*, 111, 768

Rocha-Pinto, H. J., Majewski, S. R., Skrutskie, M. F., & Crane, J. D. 2003, *ApJ*, 594, L115

Rutledge, G. A., Hesser, J. E., & Stetson, P. B. 1997a, *PASP*, 109, 907

Rutledge, G. A., Hesser, J. E., Stetson, P. B., Mateo, M., Simard, L., Bolte, M., Friel, E., & Copin, Y. 1997b, *PASP*, 109, 883

Schiavon, R. P., & Barbuy, B. 1999, *ApJ*, 510, 934

Schiavon, R. P., Barbuy, B., Rossi, S. C. F., & Milone, A. 1997, *ApJ*, 479, 902

Searle, L., & Zinn, R. 1978, *ApJ*, 225, 357

Stanek, K. Z., & Garnavich, P. M. 1998, *ApJ*, 503, L131

Tonry, J., & Davis, M. 1979, *AJ*, 84, 1511

VandenBerg, D. A., Bergbusch, P. A., & Dowler, P. D. 2006, *ApJS*, 162, 375

Walterbos, R. A. M., & Kennicutt, R. C., Jr. 1987, *A&AS*, 69, 311

Walterbos, R. A. M., & Kennicutt, R. C., Jr. 1988, *A&A*, 198, 61

White S. D. M., & Rees, M. J. 1978, *MNRAS*, 183, 341

Worthey, G., Espana, A., MacArthur, L. A. & Courteau, S. 2005, *ApJ*, submitted (astro-ph/0410454)

Yanny, B., et al. 2003, *ApJ*, 588, 824

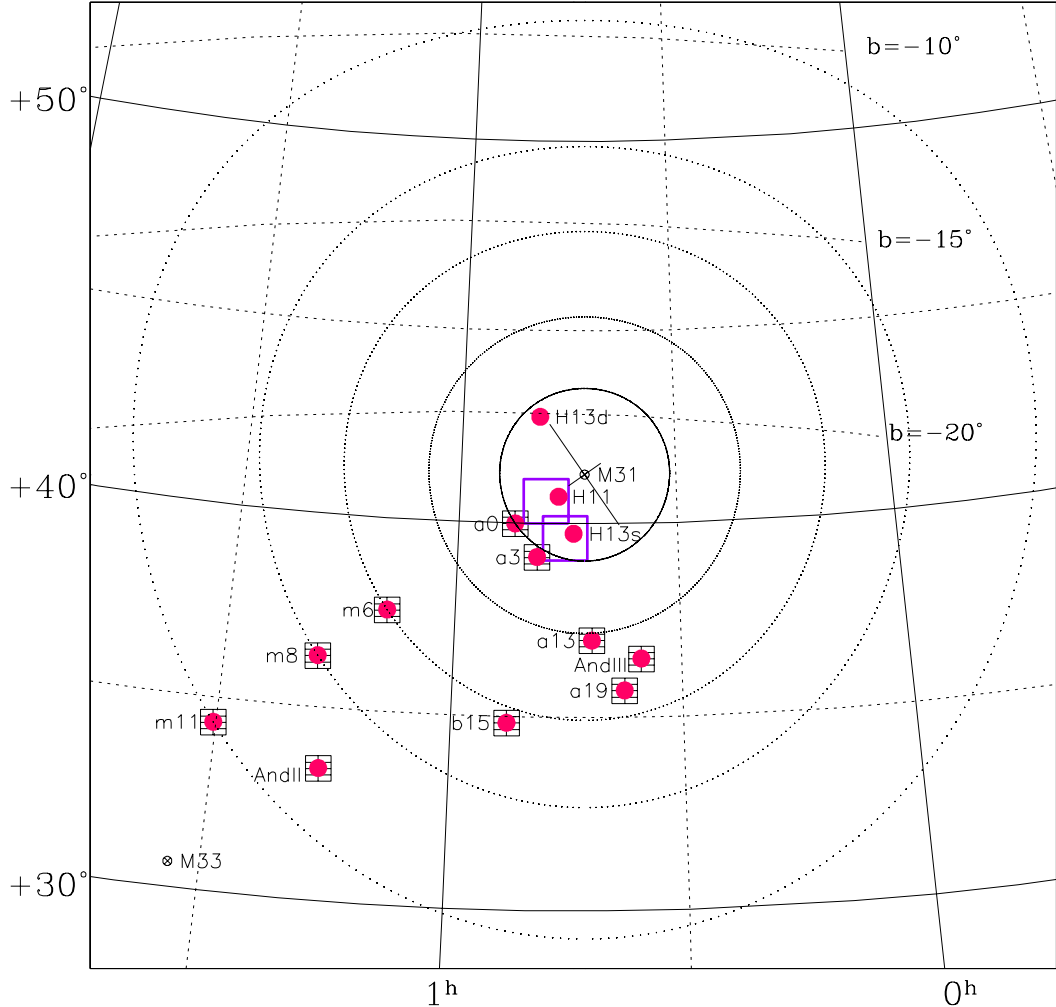


Fig. 1.— Sky position (J2000.0 RA/DEC) of the fields observed with DEIMOS spectroscopic slitmasks (solid circles). The small gridded squares indicate the full area ($35' \times 35'$) of the fields from the KPNO 4-m/Mosaic imaging survey of Ostheimer (2002). The resulting photometric *DDO51*-, *M*-, and *T*₂-band catalog was used to select spectroscopic targets for the DEIMOS slitmasks, each of which covers an area of roughly $16' \times 4'$. The majority of the fields in our *DDO51* survey lie close to the south-eastern minor axis of M31 and extend out to a projected distance from M31 of $R = 163$ kpc (field m11). The large bold open squares represent two of our CFHT MegaCam *g'*- and *i'*-band pointings, used to select spectroscopic targets for fields H11 and H13s. The pair of thin solid diagonal lines indicates the approximate extent of the visible disk of M31. The location of M33 is marked near the lower left. The concentric circles correspond to projected distances from M31’s center of 30, 60, 90, 120, and 165 kpc. A few lines of Galactic latitude are also marked.

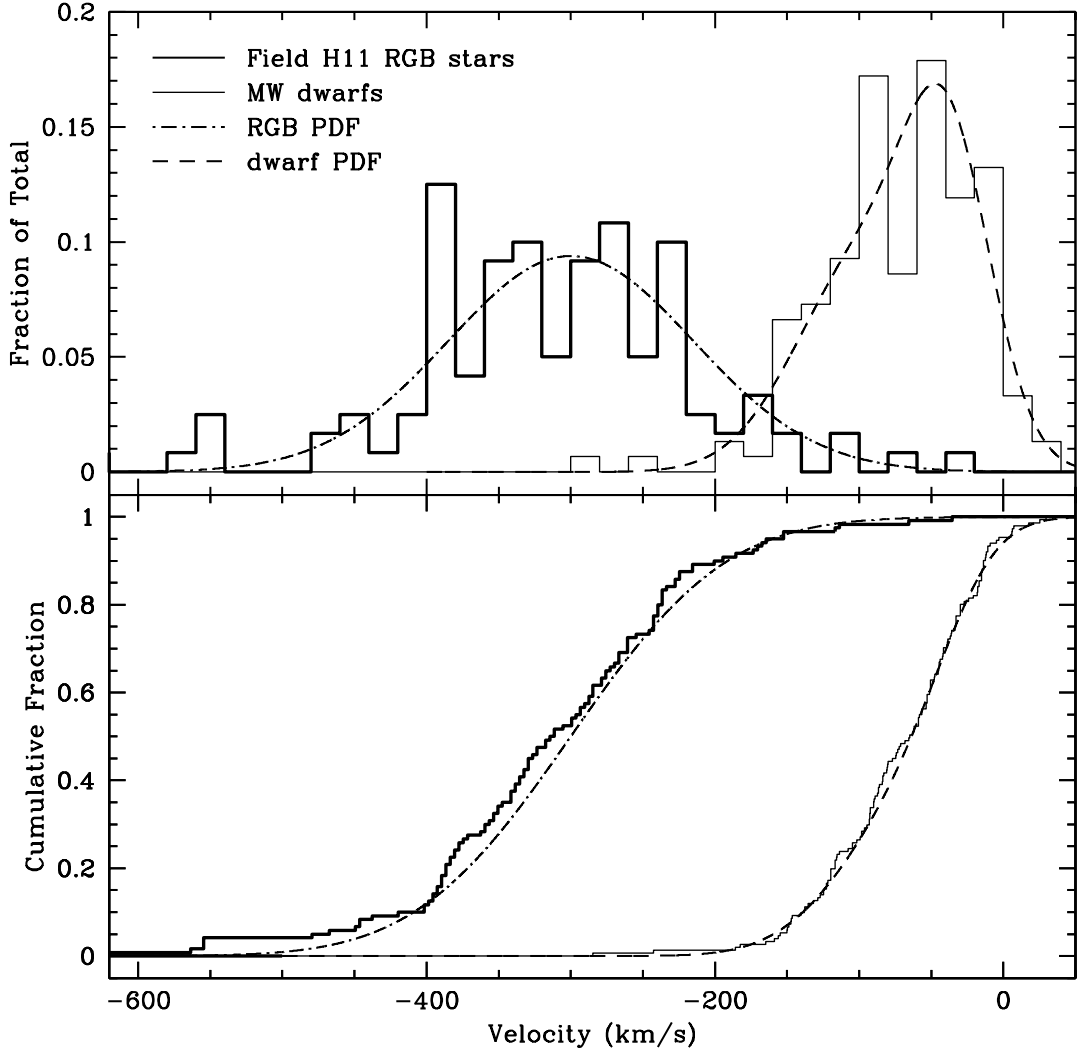


Fig. 2.— Probability distribution functions for radial velocity in differential (*top*) and cumulative (*bottom*) form. The thin-lined histograms show the dwarf star training set; the dashed curves show the double Gaussian fit used to define the PDF. Since the red giant branch training set is selected on the basis of radial velocity, it cannot be used to define the radial velocity PDF. We instead adopt a Gaussian as the RGB PDF (dot-dashed curve), centered on M31’s systemic velocity of -300 km s^{-1} with a width of $\sigma = 85 \text{ km s}^{-1}$, based on a fit to the inner spheroid field H11 sample (bold solid histograms). Dwarf stars lie close to $v_{\text{hel}} \sim 0 \text{ km s}^{-1}$ but have a negative tail due to the reflex of the component of the Sun’s velocity towards M31. As such, there is substantial overlap between the M31 RGB and MW dwarf radial velocity distributions.

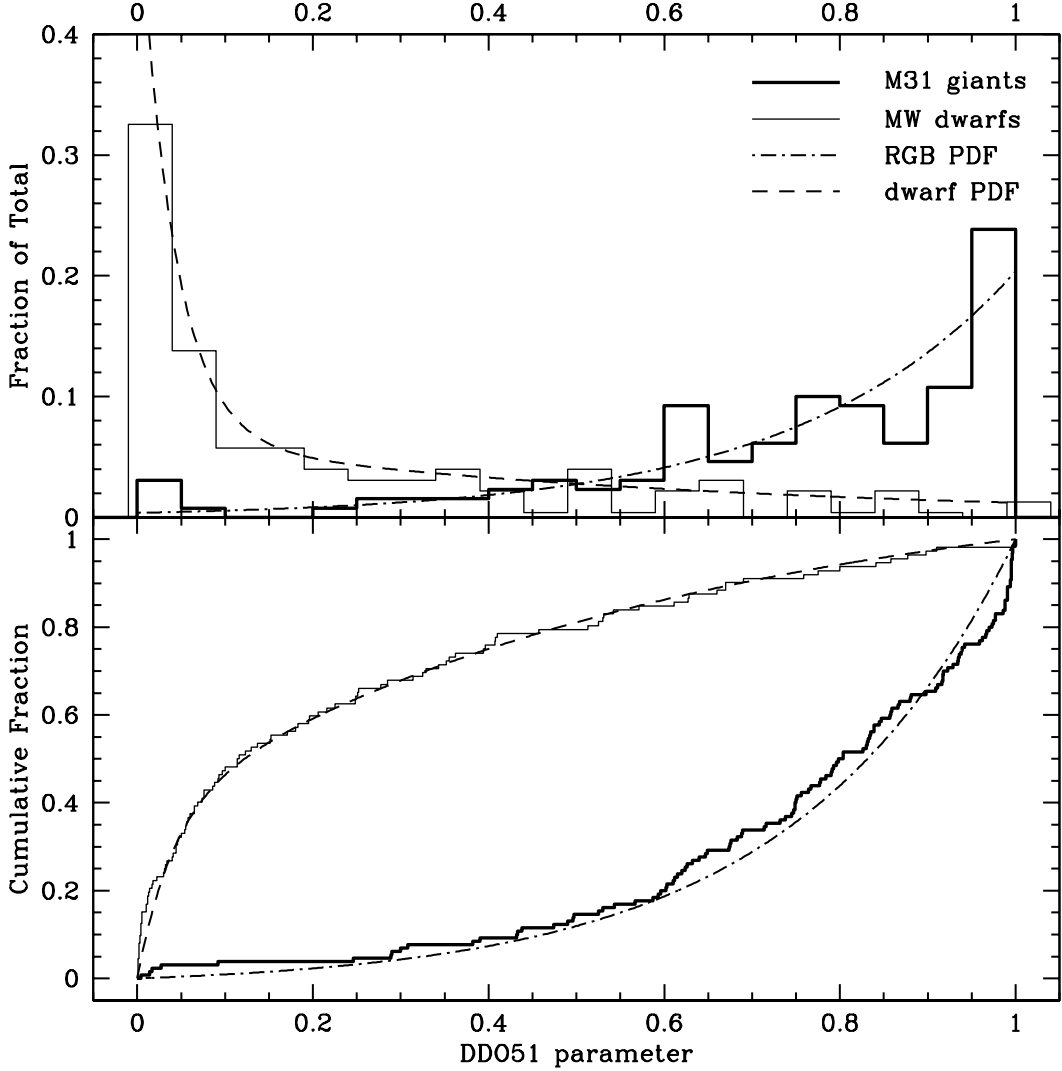


Fig. 3.— Same as Figure 2 for the DDO51 parameter. The bold solid histograms represent the RGB training set, a compilation of RGB stars from several fields close to M31’s center. The DDO51 parameter is assigned based on the position of a star in the $(M - DDO51)$ vs. $(M - T_2)$ color-color diagram (Majewski et al. 2000): a value close to zero implies it is likely to be a dwarf star whereas a value close to unity implies it is likely to be an RGB star. The photometry is from KPNO 4-m Mosaic images in the Washington system M and T_2 bands and in the intermediate-width DDO51 band, which includes the surface-gravity sensitive Mg b and MgH stellar absorption features at ~ 5100 Å. Exponential fits to the dwarf and RGB training sets are used to define the PDFs. As expected, the MW dwarf training set distribution peaks at zero and that of the RGB training set peaks at unity, but there is significant overlap between the two distributions.

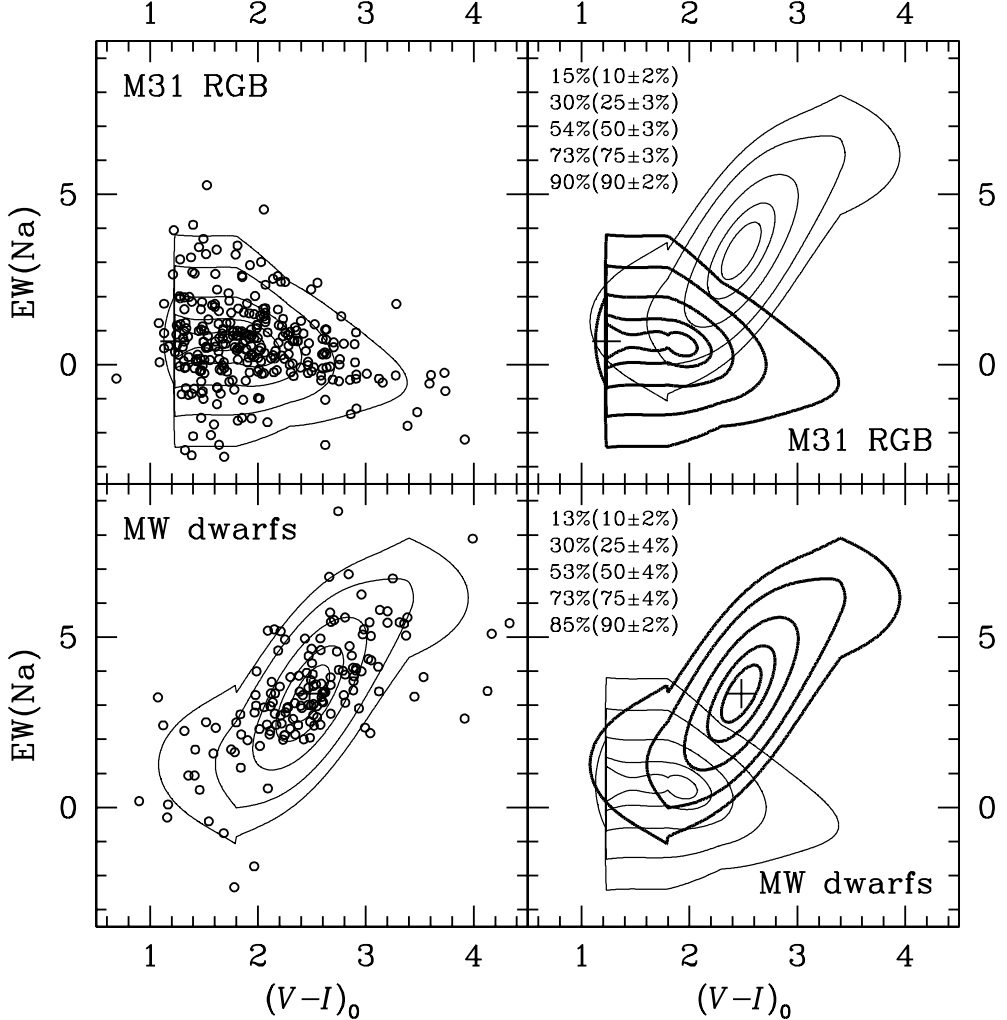


Fig. 4.— Two-dimensional PDFs for the equivalent width of the surface-gravity-sensitive Na I absorption line doublet at 8190 Å as a function of dereddened $(V-I)_0$ color (which is sensitive to stellar effective temperature). The left panels show iso-probability contours for the RGB (*top*) and dwarf (*bottom*) PDFs, which are analytic fits to the distribution of training set stars (open circles). Both sets of PDF contours are shown in the right panels with the RGB and dwarf contours in bold in the top and bottom panels, respectively. The percentage of training set stars enclosed within each contour is indicated in the right panels (ordered from innermost to outermost); the percentage of analytic PDF space enclosed by the contour and the Poisson error are listed within parentheses. Cool dwarf stars with $(V-I)_0 > 2$ exhibit strong Na I absorption, while RGB and hotter dwarf stars show negligible Na I absorption. The color distribution of M31 RGB training set stars is asymmetric; it peaks at $(V-I)_0 \gtrsim 1$ but has a tail extending out to redder colors. The MW dwarf training set stars have a somewhat broader and symmetric color distribution centered on $(V-I)_0 \approx 2.5$. The Na I diagnostic is very effective at separating M31 RGB stars from MW dwarfs for stars redder than $(V-I)_0 \sim 2.5$, but cannot distinguish between the two stellar types for $(V-I)_0 \lesssim 2$.

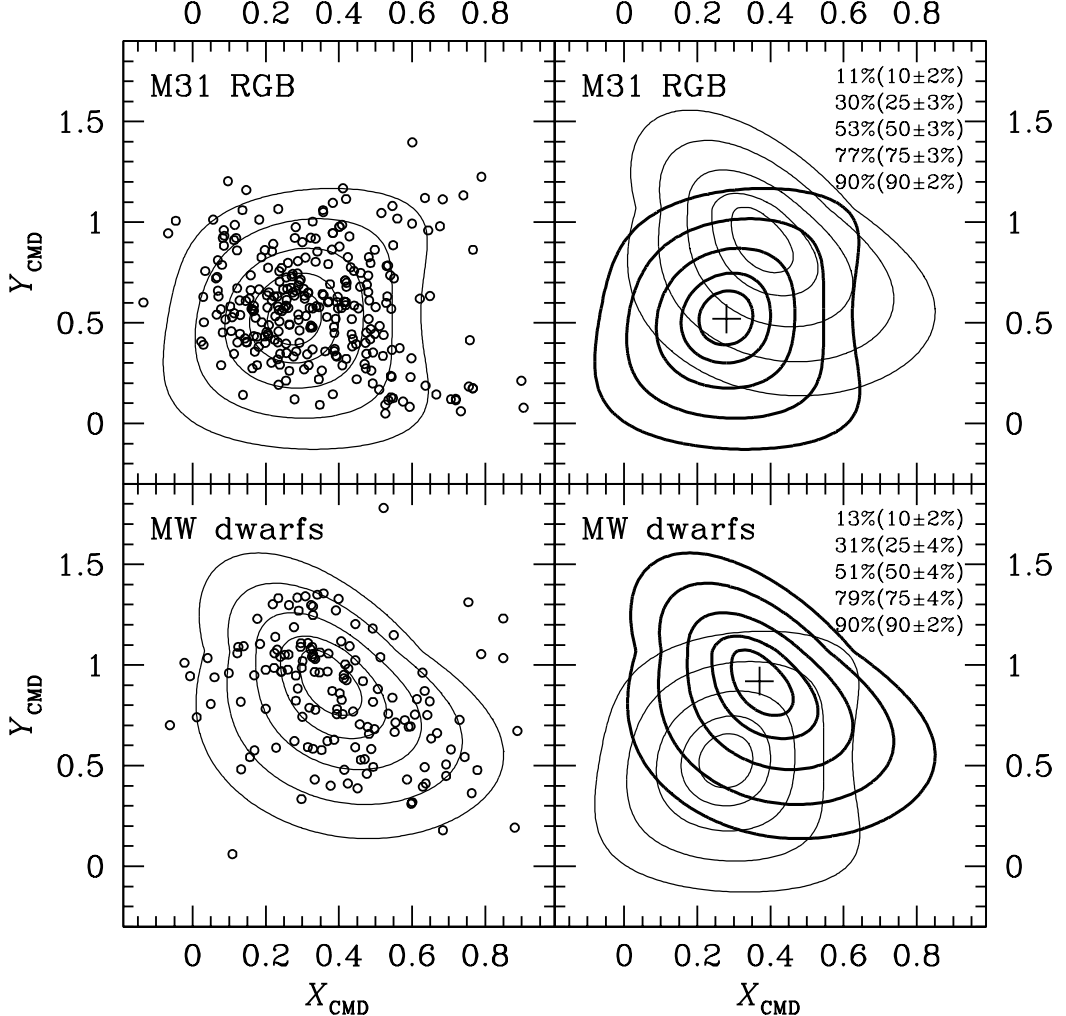


Fig. 5.— Same as Figure 4 for position within the $(I, V - I)$ color-magnitude diagram. The abscissa is the fractional distance across the isochrones: $X_{\text{CMD}} = 0$ at the most metal-poor isochrone, $[\text{Fe}/\text{H}] = -2.6$, and $X_{\text{CMD}} = 1$ at the most metal-rich isochrone, $[\text{Fe}/\text{H}] = +0.5$; the ordinate is the fractional distance along the RGB isochrones: $Y_{\text{CMD}} = 0$ at $I_0 = 22.5$, at the faint end of our spectroscopic sample, and $Y_{\text{CMD}} = 1$ at the tip of the RGB. These parameters are calculated using theoretical RGB isochrones from Vandenberg et al. (2006), for an age of $t = 12$ Gyr and chemical composition of $[\alpha/\text{Fe}] = 0$, shifted to M31’s distance modulus of 24.47 mag. Since M31 RGB stars tend to occupy the region of the CMD that is bounded by the isochrones (widest color spread near the tip of the RGB, progressively smaller color spread toward fainter I_0 magnitudes), they form a roughly rectangular locus in $(X_{\text{CMD}}, Y_{\text{CMD}})$ space. On average, foreground dwarf stars tend to be brighter in I_0 than M31 RGB stars. Dwarfs are broadly distributed in the $(I, V - I)$ CMD, but since the RGB isochrones curve toward redder colors as metallicity increases and tend to be more widely separated toward the tip of the RGB, dwarf stars at higher Y_{CMD} values tend to have a lower mean X_{CMD} and smaller spread in X_{CMD} .

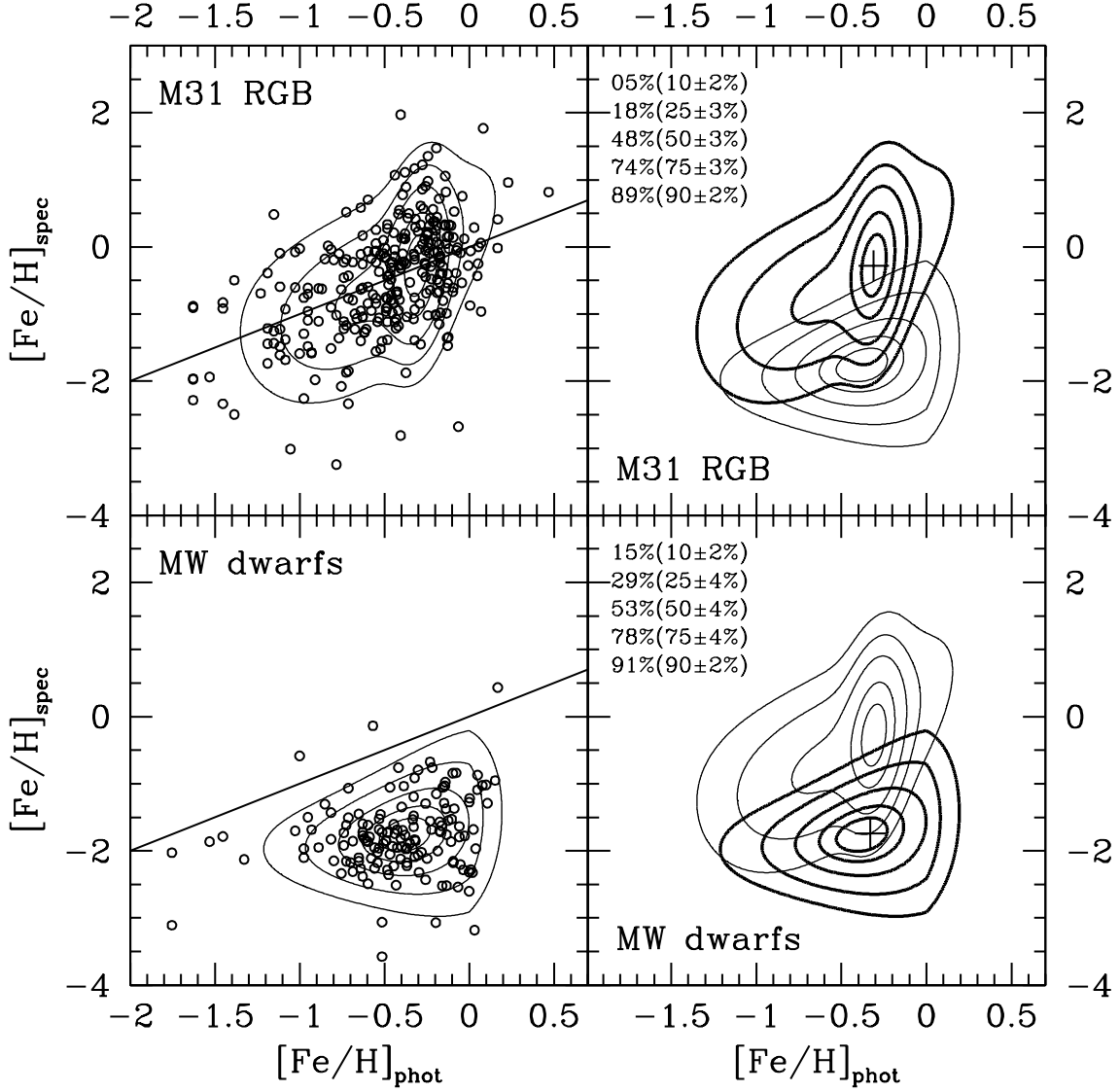


Fig. 6.— Same as Figure 4 for photometric versus spectroscopic metallicity estimates. The $[\text{Fe}/\text{H}]_{\text{phot}}$ estimate is derived by comparing the CMD position of each star to 12.6 Gyr model isochrones with $[\alpha/\text{Fe}] = 0$ spanning a wide range of metallicities (Vandenberg et al. 2006). The $[\text{Fe}/\text{H}]_{\text{spec}}$ estimate is derived from the equivalent width of the Ca II triplet absorption feature at $\sim 8500 \text{ \AA}$, using empirical calibration relations based on Galactic globular cluster red giants (Rutledge et al. 1997a,b). M31 RGB stars show reasonable agreement between $[\text{Fe}/\text{H}]_{\text{phot}}$ and $[\text{Fe}/\text{H}]_{\text{spec}}$, as expected. The $[\text{Fe}/\text{H}]_{\text{phot}}$ estimate for dwarf stars is obviously incorrect, as it is based on RGB isochrones at the distance of M31; dwarf stars tend to have relatively weak Ca II lines and generally lie well below the $[\text{Fe}/\text{H}]_{\text{phot}} = [\text{Fe}/\text{H}]_{\text{spec}}$ relation (diagonal lines in left panels).

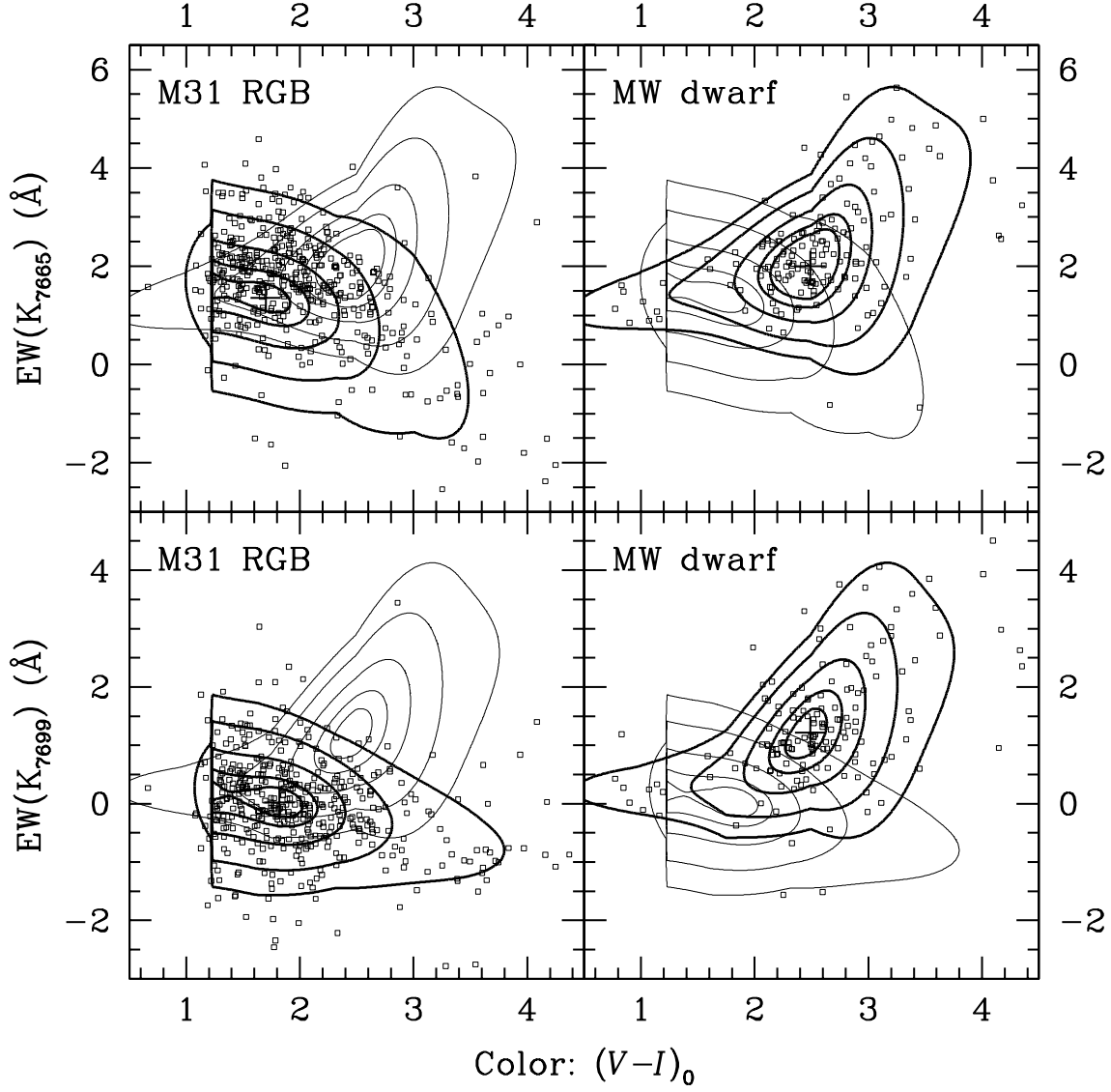


Fig. 7.— Similar to Figure 4 for the K_I 7665 Å (top) and 7699 Å (bottom) lines. Data points show M31 RGB (left) and M31 dwarf (right) stars from the final training set overlaid on both sets of PDF contours, with the corresponding set of contours in bold. There is significant overlap between the M31 RGB and MW dwarf distributions for bluer colors [$(V - I)_0 > 2.5$]. However, the strength of the K_I absorption lines increases with increasing $(V - I)_0$ for dwarf stars, leading to a clear differentiation between the two stellar types at redder colors.

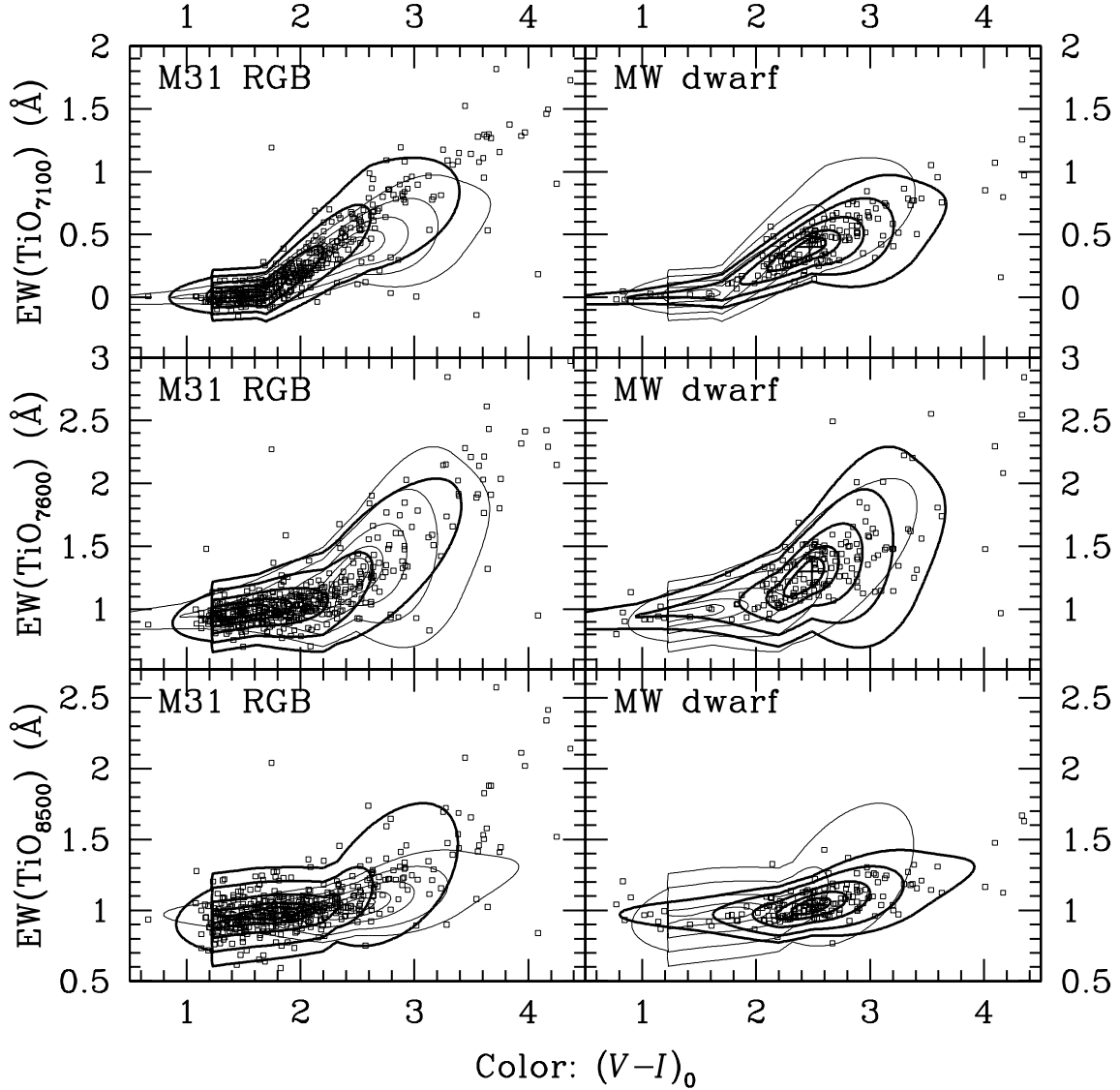


Fig. 8.— Same as Figure 7 for the TiO 7100, 7600, and 8500 Å bands (*top*→*bottom*), with the RGB and dwarf training set stars and PDFs shown in the left and right panels, respectively. There is substantial overlap between the RGB and dwarf PDFs, especially for the TiO 7600 Å band for which the measurements are complicated by the presence of the telluric A band. No TiO bands are present for relatively hot stars with $(V - I)_0 \lesssim 2.0$, so the diagnostics provide no RGB/dwarf discrimination in this regime. However, the TiO strengths of dwarf and RGB stars follow two slightly different increasing trends with increasing $(V - I)_0$, so that these diagnostics have some power for stars redder than $(V - I)_0 \gtrsim 2.0$.

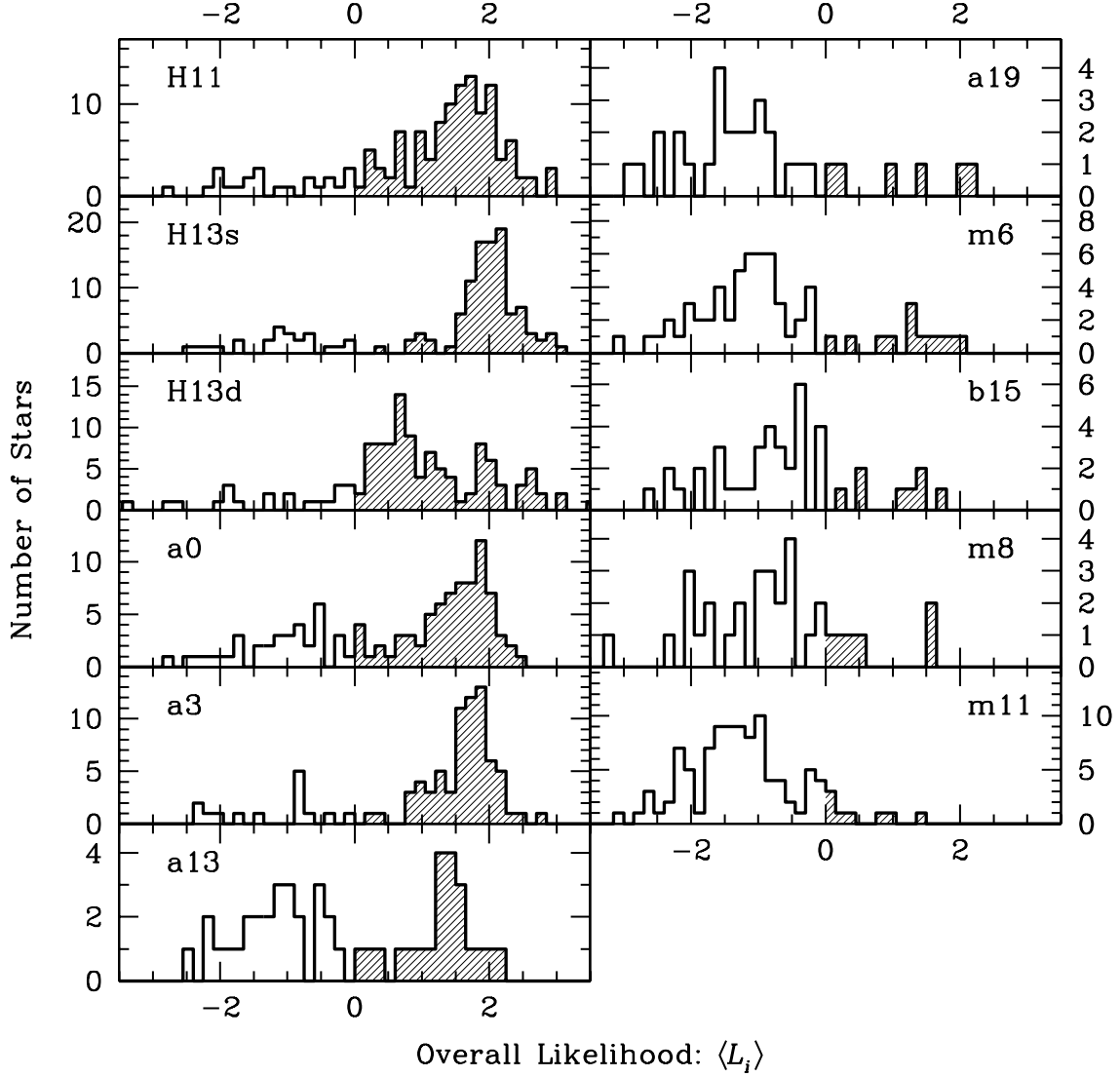


Fig. 9.— Histograms of overall likelihood ($\langle L_i \rangle$) values, where $L_i = \log(P_{\text{giant}}/P_{\text{dwarf}})$ for each diagnostic, for stars in the M31 outer halo fields. The fields are arranged in order of increasing projected distance from M31 (see Fig. 1). Confirmed RGB stars are those with $\langle L_i \rangle > 0$ (shaded histograms) while $\langle L_i \rangle < 0$ indicates dwarf stars (open histograms). There are clear peaks at $\lesssim -1$ and $\gtrsim +1$, indicating RGB and dwarf star distributions respectively: in fields with approximately equal numbers of RGB and dwarf stars, there is a clear bimodality (e.g., fields a0 and a13). In inner fields there is a clear RGB peak with a tail of dwarf stars, while in outer fields there is a clear dwarf peak with a tail of RGB stars. As expected, the red giant fraction decreases with increasing distance from M31. The exception is field a3, which due to the increased RGB density in the southern stream has significantly fewer dwarf stars. We find secure RGB stars all the way out to field m11, which has three distinct outliers (M31 RGB stars) from the main distribution (Galactic dwarf stars).

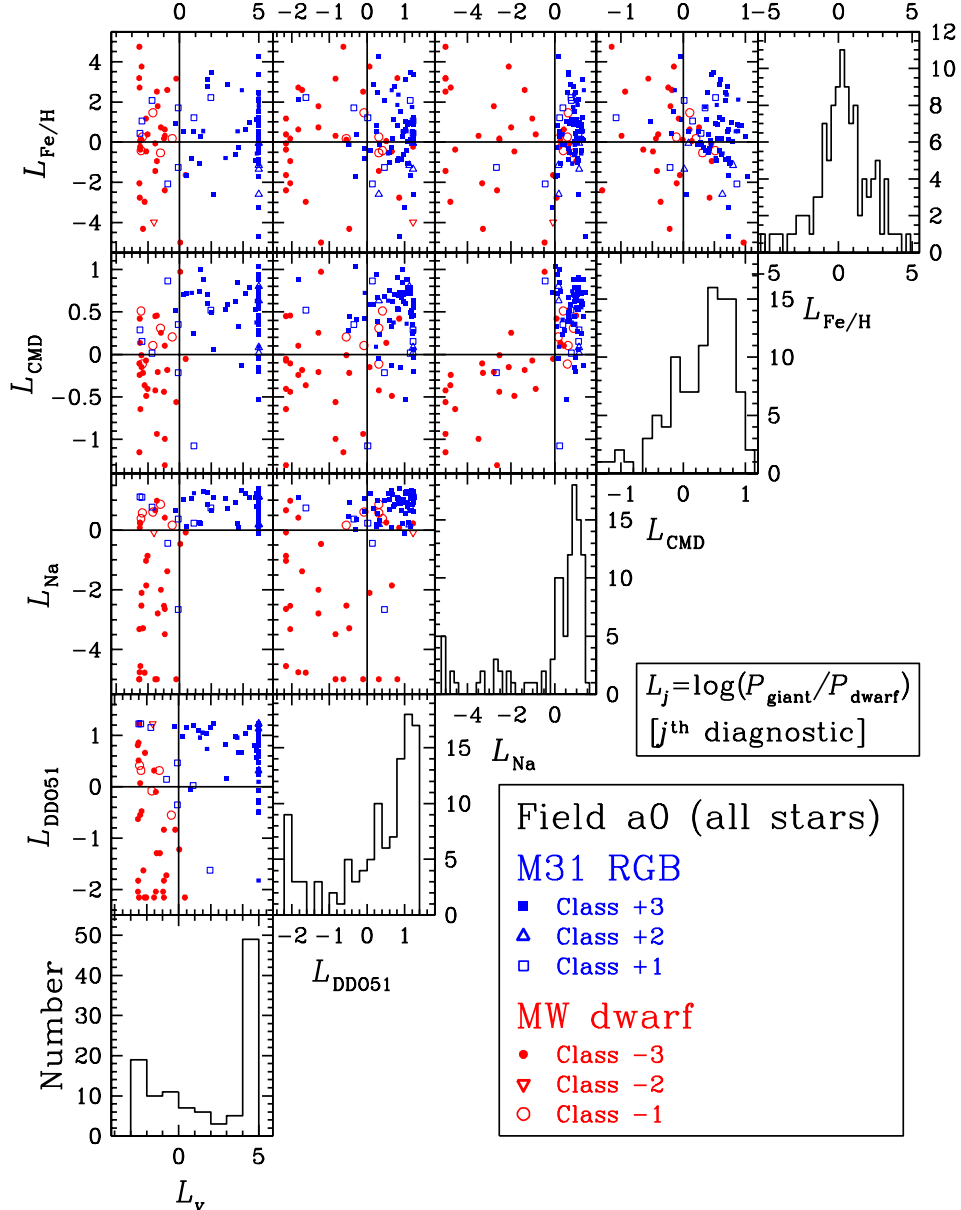


Fig. 10.— The position of all stars in field a0 at $R = 30$ kpc in probability ratio space for the five primary diagnostics. The panels along the right edge diagonal show histograms of $L_j = \log(P_{\text{giant}}/P_{\text{dwarf}})$ for each diagnostic j ; positive values indicate the star is more likely to be an RGB star than a dwarf (in terms of that diagnostic) and vice versa for negative values. The blue and red symbols indicate M31 RGB stars and MW dwarfs, respectively, as determined by our likelihood-based method (§ 3.5) and are subdivided into: Class ± 3 (very secure: filled symbols), Class ± 2 (secure: triangles), and Class ± 1 (marginal: open squares/circles). It is reassuring to see that most RGB stars lie in the top right quadrant of the L_j vs. L_k panels, while most dwarf stars lie in the bottom left quadrant. While no single diagnostic is a perfect RGB/dwarf discriminant, their combination is very effective at separating these two populations.

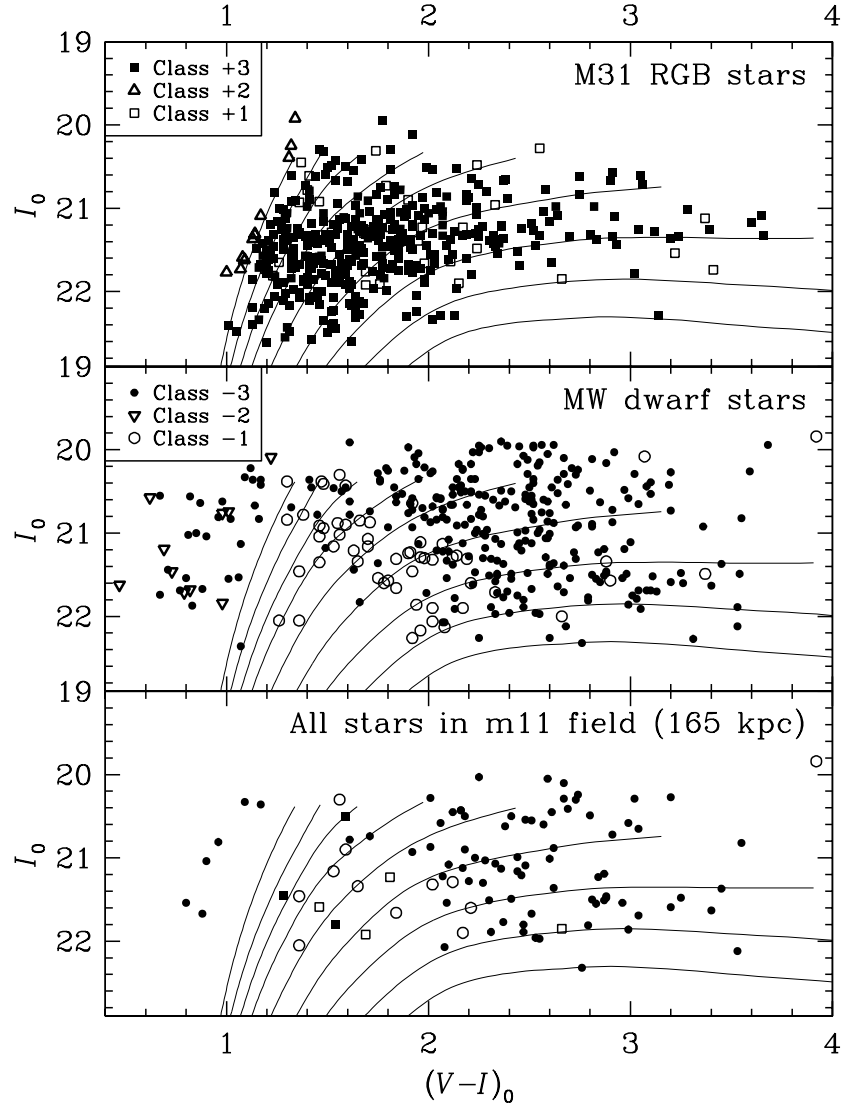


Fig. 11.— Color-magnitude diagram of: (top) RGB stars from all fields with classes +3, +2, and +1 represented by filled squares, open triangles, and open squares, respectively (in order of decreasing certainty of classification; see § 3.5), (middle) all dwarf stars with classes -3, -2, and -1 represented by filled circles, inverted open triangles, and open circles, respectively, and (bottom) all stars in our outermost field m11 with the same symbols as above representing the different classes. The thin curves in each panel show theoretical RGB tracks from Vandenberg et al. (2006) for an age of 12 Gyr, $[\alpha/\text{Fe}] = 0$, and metallicities (from left to right) of $[\text{Fe}/\text{H}] = -2.3, -1.7, -1.3, -1.0, -0.7, -0.4, -0.1, +0.1$, and $+0.4$.

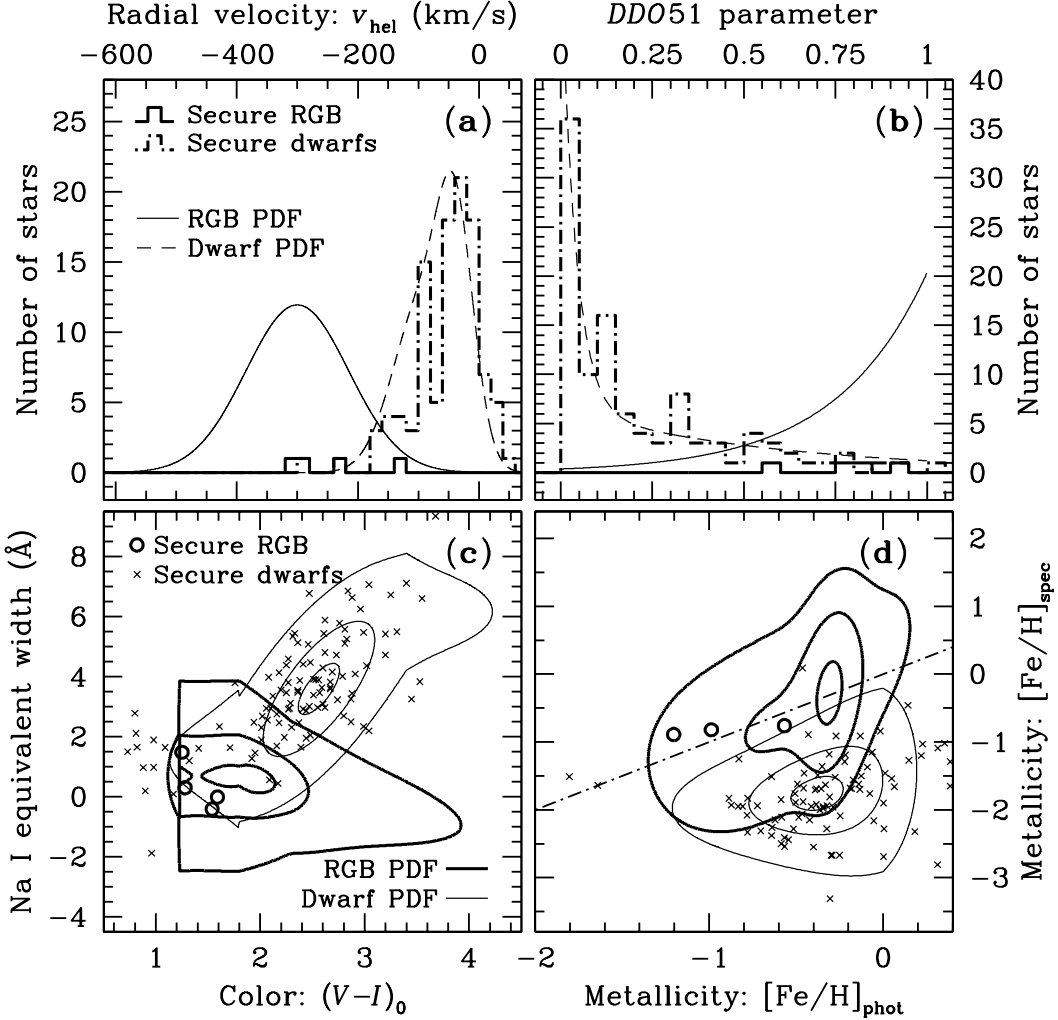


Fig. 12.— (a) Radial velocity histograms for M31 RGB and MW dwarf stars in our two outermost fields m8 and m11. Confirmed RGB stars are represented by the bold solid histogram and secure Galactic dwarf stars by the bold dot-dashed histogram. The RGB PDF is shown as a solid curve, and the dwarf PDF is shown as a dashed curve (Fig. 2). The stars were classified as secure RGB or dwarf stars by use of the five-diagnostic method. The RGB and dwarf PDFs are normalized to the same area but the normalization has not been adjusted to match the actual number of stars. (b) Same as (a) for the DDO51 parameter (see Fig. 3). (c) Same as (a) for $(V - I)_0$ vs. Na I EW for secure RGB stars (bold open circles) and dwarfs (crosses) in our two outermost fields. The RGB and dwarf two-dimensional PDF contours are shown as bold and thin lines, respectively (see Fig. 4). (d) Same as (c) for $[\text{Fe}/\text{H}]_{\text{phot}}$ vs. $[\text{Fe}/\text{H}]_{\text{spec}}$ (see Fig. 6). The dot-dashed diagonal line shows the $[\text{Fe}/\text{H}]_{\text{spec}} = [\text{Fe}/\text{H}]_{\text{phot}}$ line. Only three RGB stars are shown; the fourth is a significant outlier with respect to both PDFs so this diagnostic received very little weight in the overall likelihood computation for this star (Eq. 8).

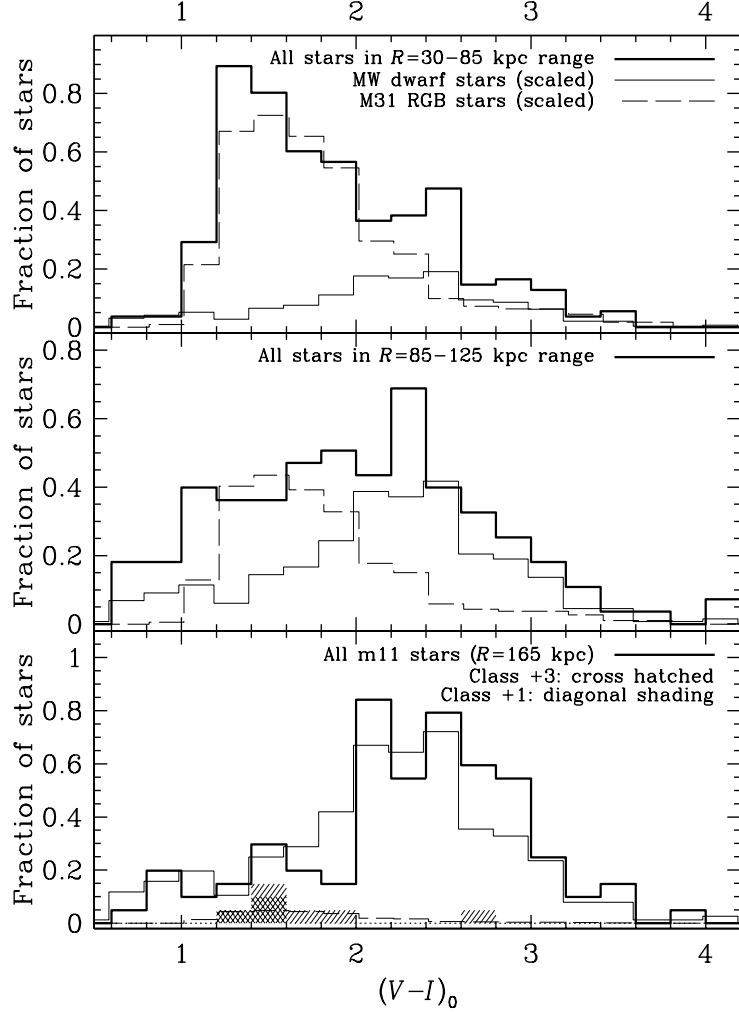


Fig. 13.— (Top) The $(V - I)_0$ color distribution of all stars in fields in the radial range $R = 30\text{--}85$ kpc (bold histogram). This distribution is best fit by a 75%/25% combination of the color distributions of secure+marginal M31 RGB (Class > 0) and MW dwarf (Class < 0) stars (thin dashed and thin solid histograms, respectively). (Middle) Same as (top) for all stars in fields in the radial range $R = 85\text{--}125$ kpc. The best fit in this case is an approximately equal mix of M31 RGB and MW dwarf stars, 45%/55%. (Bottom) Same as (top) for all stars in our remotest M31 halo field m11 at $R = 163$ kpc. The m11 stellar $(V - I)_0$ color distribution generally follows that of secure+marginal MW dwarf stars. The $(V - I)_0$ colors of all three Class +3 stars and three of the four Class +1 stars in m11 (cross-hatched and diagonally shaded histograms, respectively) coincide with the peak of the color distribution of secure+marginal M31 RGB stars. These stars form a slight apparent peak at $(V - I)_0 \sim 1.5$, but the peak is not statistically significant; in other words, these stars would not have been identified as M31 RGB stars on the basis of the color distribution alone, but they are identified by our likelihood method. A 5%/95% combination of M31 RGB and MW dwarf stars is shown.

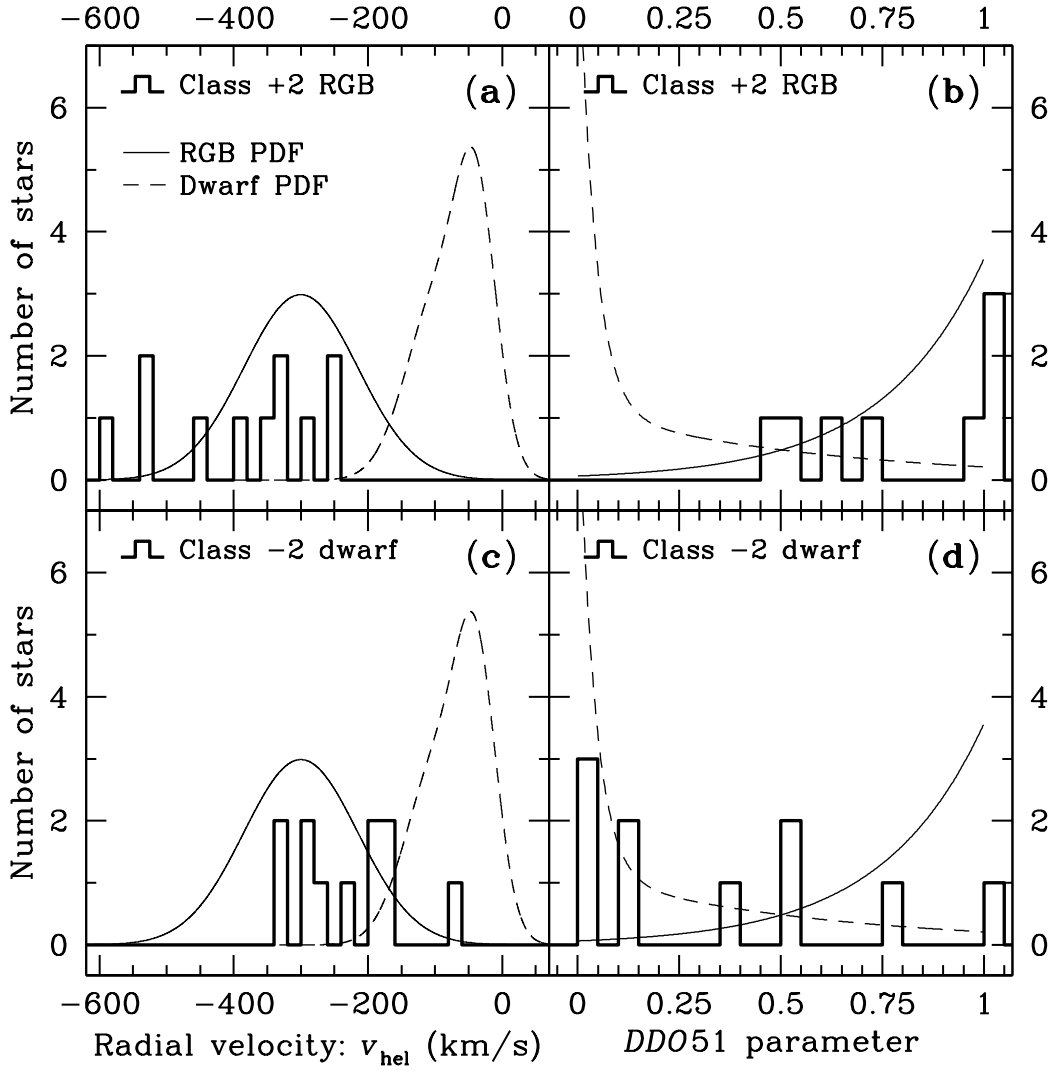


Fig. 14.— (a–b) Same as Figure 12(a–b) for Class +2 M31 RGB stars as defined in § 3.5 (bold histogram). The distribution of radial velocities and DDO51 parameters for these stars is a far better match to the RGB PDF (thin solid curve) than to the dwarf PDF (thin dashed curve). (c–d) Same as (a–b) for Class –2 MW dwarf stars (bold histogram).

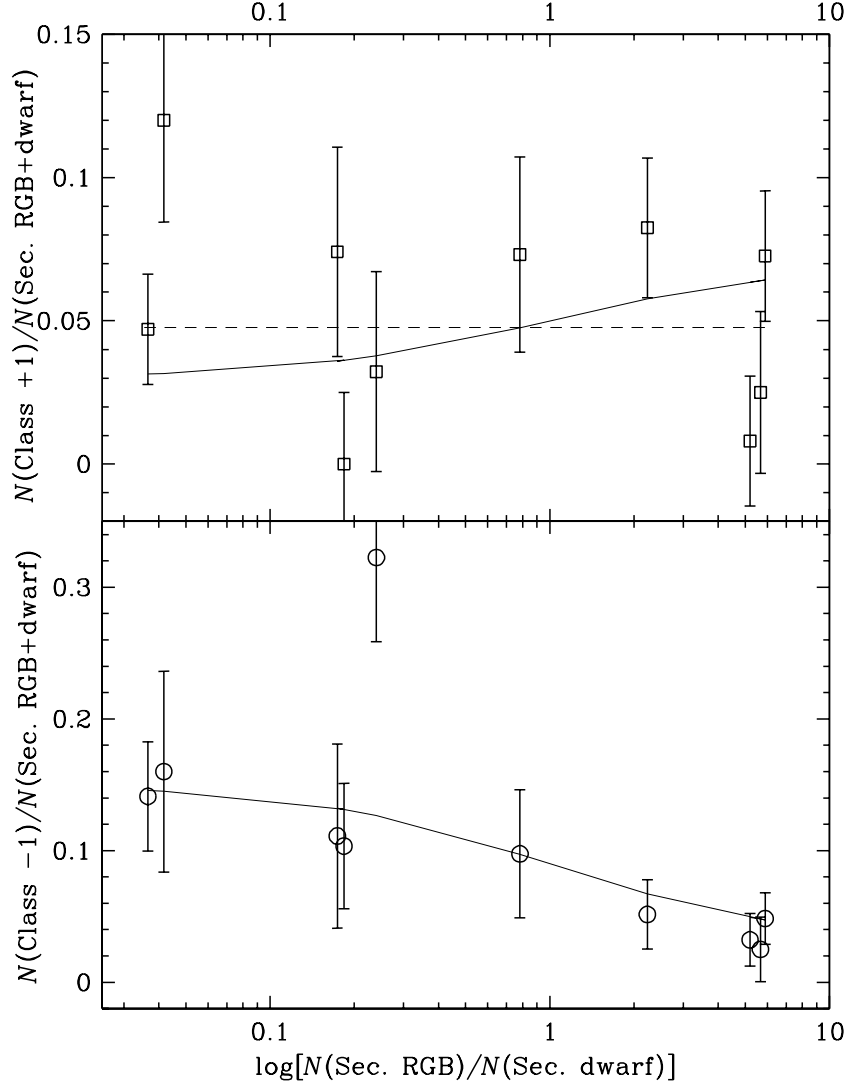


Fig. 15.— (Top) Ratio of the number of marginal M31 RGB (Class +1) stars to the number of secure RGB+dwarf stars plotted as a function of the ratio of secure RGB to dwarf stars. Each data point represents one of our fields (since the ratio of secure RGB to dwarf stars increases with decreasing radius, the fields are roughly ordered inversely by radius along the x axis). The thin solid curve is a model in which the Class +1 stars are a specific mix of RGB and dwarf stars ($a = 0.07$ and $b = 0.03$; see § 4.1.3). The Poisson error bars shown are based on this model. An alternate model, $a = b = 0.05$, is shown as a horizontal thin dashed line. (Bottom) Same as (top) for marginal MW dwarf (Class -1) stars. The thin solid curve is a model with mix parameters $c = 0.03$ and $d = 0.15$.

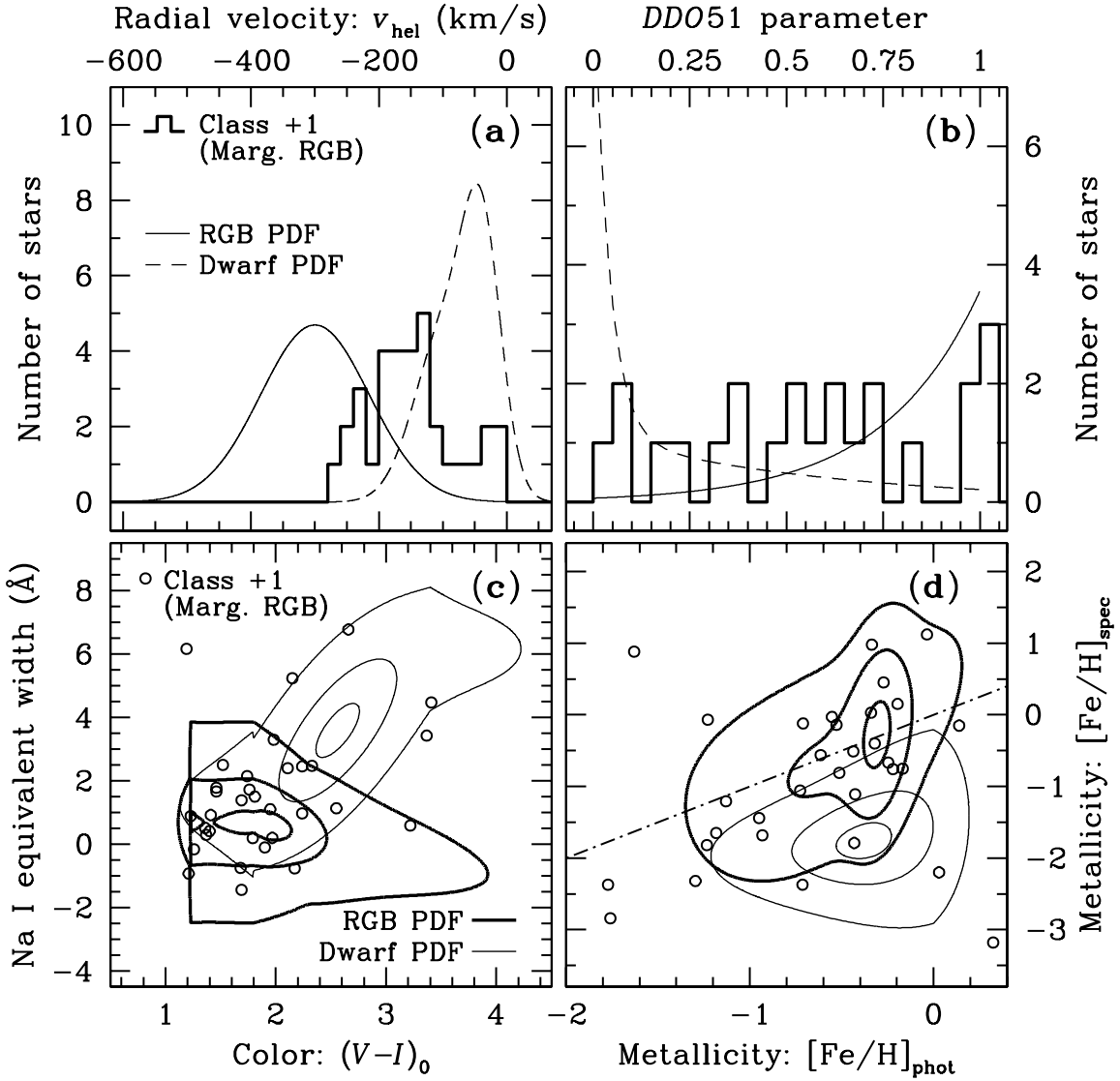


Fig. 16.— Same as Figure 12 for marginal M31 RGB (Class +1) stars (represented by bold histograms and open circles). The distribution of this sample in the four diagnostic plots indicates it consists mostly of M31 RGB stars with moderately blue colors, $(V - I)_0 \sim 1 - 2$.

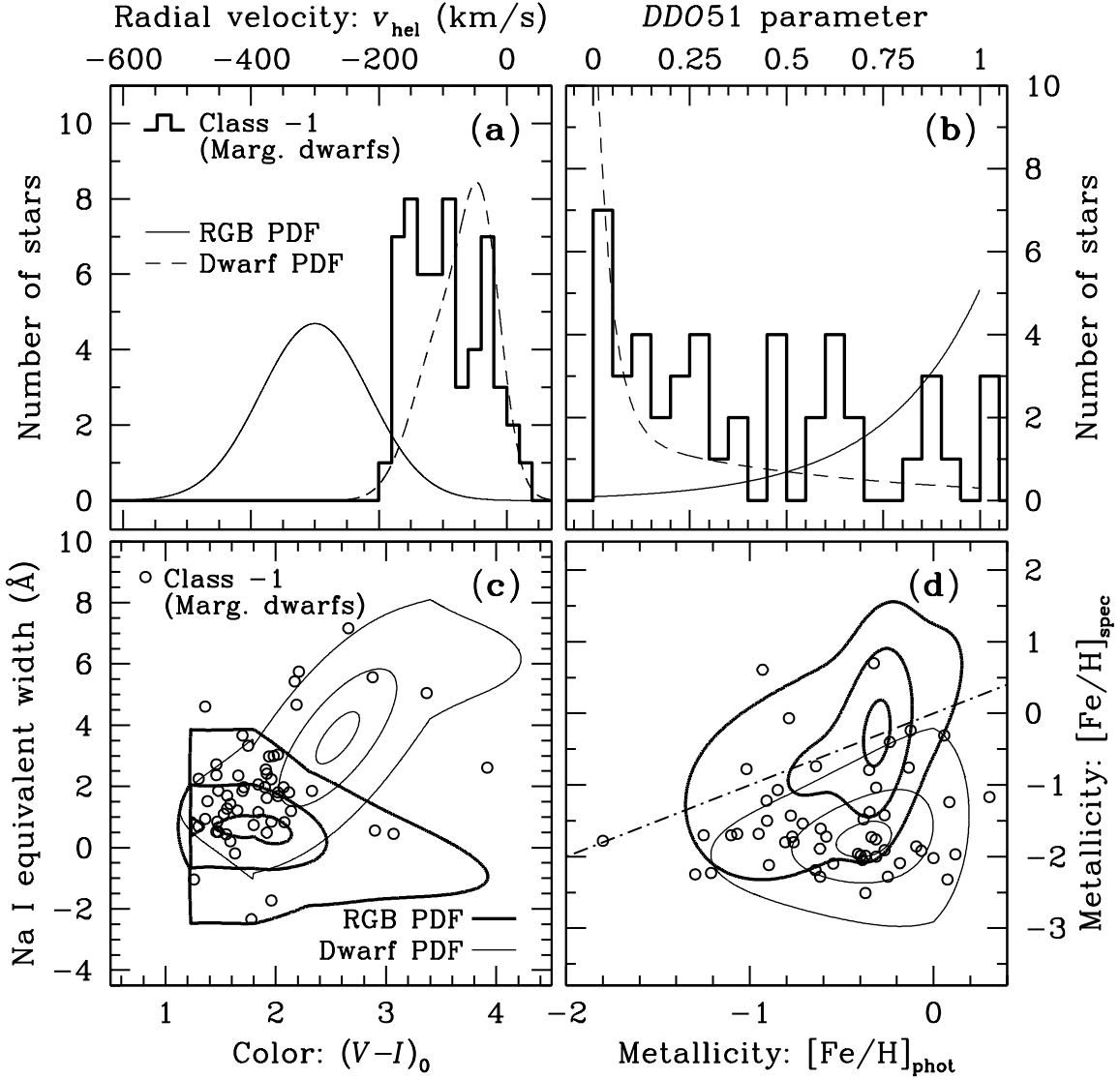


Fig. 17.— Same as Figure 16 for marginal MW dwarf (Class -1) stars (represented by bold histograms and open circles). These objects appear to be mostly MW dwarf stars with moderately blue colors, $(V - I) \sim 1 - 2$, judging from their distribution in the four diagnostic plots.

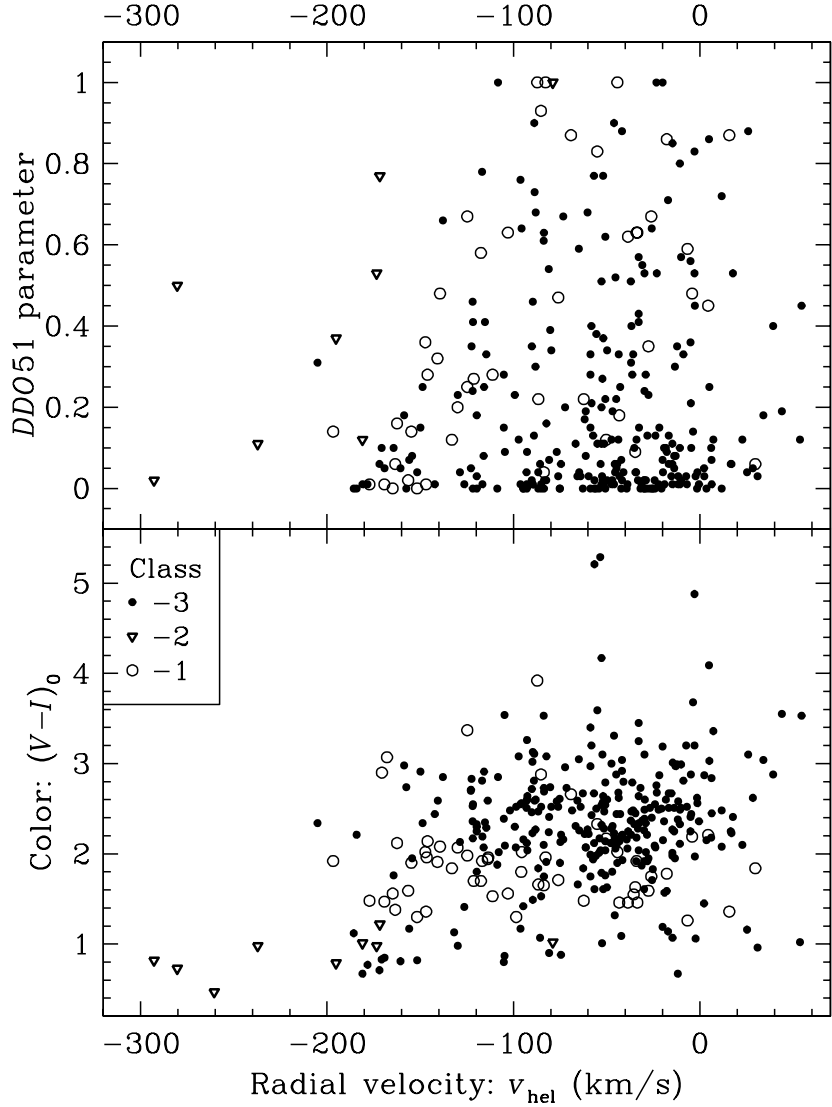


Fig. 18.— The DDO51 parameter (*top*) and $(V - I)_0$ color (*bottom*) plotted versus radial velocity for secure MW dwarf stars. As expected, dwarf stars tend to have small values of the DDO51 parameter but there is a tail to the distribution all the way up to values near unity. No significant/strong trend is seen in velocity vs. DDO51. There is a slight trend in the velocity vs. $(V - I)_0$ plot in the sense that the handful of dwarf stars with the most negative velocities are all very blue; the rest of the dwarf stars ($v \gtrsim -150$ km s $^{-1}$) span a large range of $(V - I)_0$ colors.

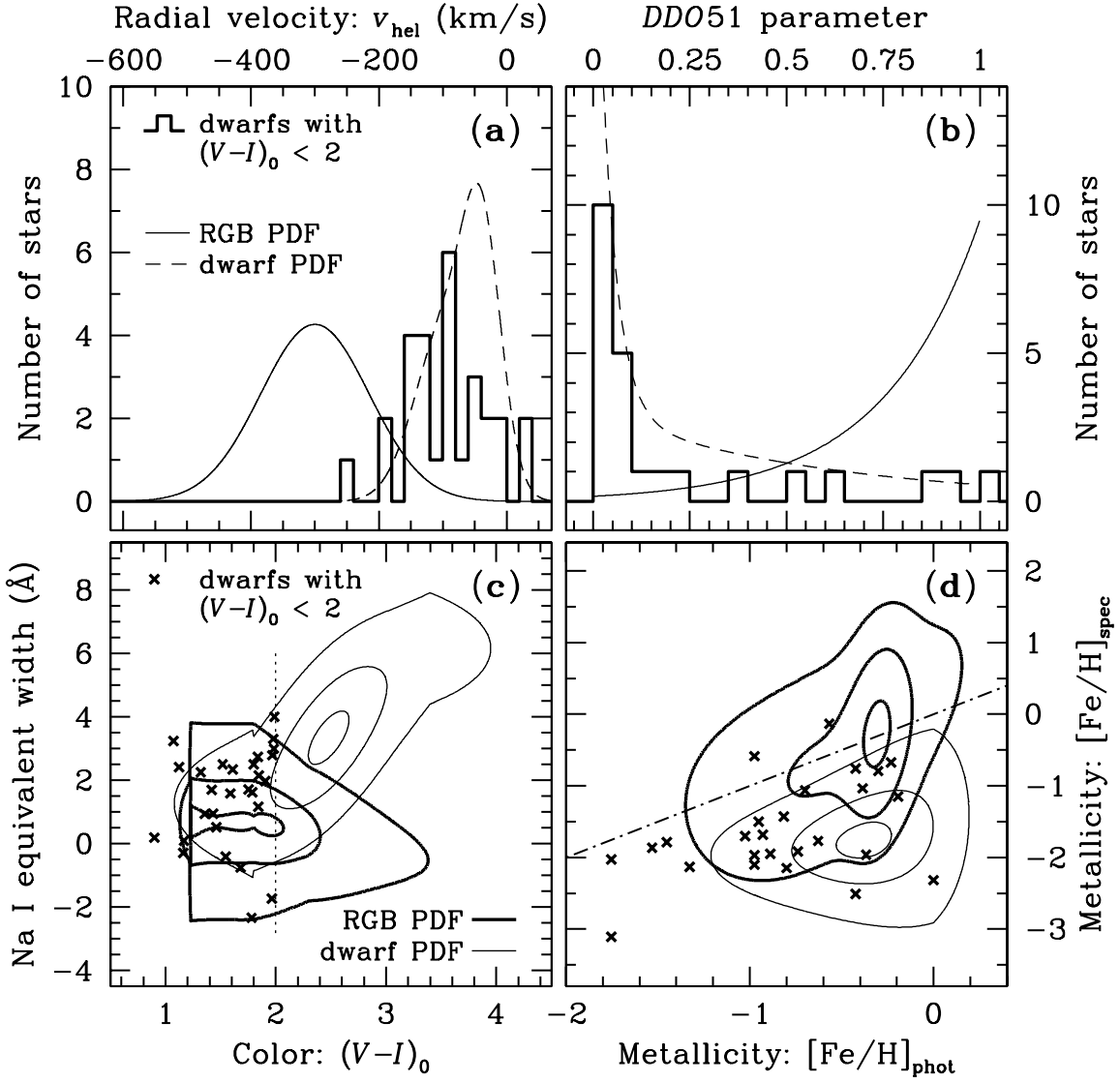


Fig. 19.— Same as Figure 12 for stars in the foreground Galactic dwarf training set with $(V - I)_0 < 2$ (represented by the bold histograms and crosses). This color cut, shown as a vertical dotted line in panel (c), is designed to isolate the tail of the training set dwarf distribution in the portion of the $(V - I)_0$ vs. Na I EW plane where the RGB and dwarf PDFs overlap. Even though the stars shown in this figure are drawn from the tail of the $(V - I)_0$ distribution, they do not show a strong bias relative to the overall dwarf distribution in the radial velocity and DDO51 diagnostic plots. There is obviously a correlation between $(V - I)_0$ and $[\text{Fe}/\text{H}]_{\text{phot}}$ (latter being based on CMD position); as a result the dwarfs in panel (d) display a bias relative to the dwarf PDF in the $[\text{Fe}/\text{H}]_{\text{phot}}$ vs. $[\text{Fe}/\text{H}]_{\text{spec}}$ plane.